

# Mantis: A Simulation-Grounded Foundation Model for Disease Forecasting

Carson Dudley\*, Reiden Magdaleno, Christopher Harding, Ananya Sharma,  
Emily Martin, Marisa Eisenberg

August 19, 2025

## Abstract

Infectious disease forecasting in novel outbreaks or low resource settings has been limited by the need for disease-specific data, bespoke training, and expert tuning. We introduce Mantis, a foundation model trained entirely on mechanistic simulations, which enables out-of-the-box forecasting across diseases, regions, and outcomes, even in settings with limited historical data. Mantis is built on over 400 million simulated days of outbreak dynamics spanning diverse pathogens, transmission modes, interventions, and surveillance artifacts. Despite requiring no real-world data during training, Mantis outperformed 39 expert-tuned models we tested across six diseases, including all models in the CDC’s COVID-19 Forecast Hub. Mantis generalized to novel epidemiological regimes, including diseases with held-out transmission mechanisms, demonstrating that it captures fundamental contagion dynamics. Critically, Mantis is mechanistically interpretable, enabling public health decision-makers to identify the latent drivers behind its predictions. Finally, Mantis delivers accurate forecasts at 8-week horizons, more than doubling the actionable range of most models, enabling proactive public health planning. Together, these capabilities position Mantis as a foundation for next-generation disease forecasting systems: general, interpretable, and deployable where traditional models fail.

## Introduction

Accurate forecasting of infectious disease dynamics is essential for effective public health response. Forecasts guide decisions around resource allocation, hospital staffing, vaccination campaigns, and non-pharmaceutical interventions such as school closures and social distancing [1, 2, 3]. Yet despite their importance, disease forecasts often fail in practice, particularly when they are most needed. During the first two years of the COVID-19 pandemic, the performance of many models in the CDC Forecast Hub was worse than a naïve baseline that simply projected the most recent value forward [4]. This highlights a key limitation of many operational systems: they struggle to provide accurate, actionable forecasts precisely when uncertainty is highest and decisions are most urgent.

Several structural limitations contribute to this breakdown. First, most models require large volumes of disease-specific historical data, which are rarely available early in outbreaks. Second, they rely on extensive manual tuning by expert teams, limiting scalability and access in under-resourced health departments, such as those in rural counties or low- and middle-income countries. Third, they generalize poorly across diseases, locations, or targets, necessitating bespoke models for every context. In addition, their forecasting horizons are typically short: most models only predict 1–4 weeks ahead [5, 6, 4], far too narrow for real-world public health planning. Key decisions, such as ramping up hospital capacity, acquiring ventilators, or coordinating vaccination campaigns, often require 6–8 weeks of lead time. Without reliable long-range forecasts, these decisions are either delayed or made reactively, often at considerable cost [7].

Many high-performing models also lack interpretability. Neural networks can capture complex outbreak dynamics, but their predictions are often opaque [5], making them difficult to trust or act upon in high-stakes

---

\* Corresponding author, cdud@umich.edu

settings. This reflects a broader divide in the modeling landscape: mechanistic models offer transparency and domain alignment, but struggle with accuracy and adaptability. Machine learning models can deliver flexible, high-performance forecasts, but operate as black boxes. Public health decision-makers are not machine learning experts; they require forecasts that are not only accurate, but explainable in epidemiological terms. Without this, even good predictions may be dismissed or misunderstood. Bridging this gap requires tools that connect model behavior to domain-relevant mechanisms, such as transmission rates, reporting delays, or immunity waning. Enabling this kind of mechanistic interpretability could transform disease forecasting from a black-box tool into a trusted decision aid.

Simulation-Grounded Neural Networks (SGNNs) provide a framework for overcoming these challenges [8]. SGNNs learn entirely from large-scale, highly realistic mechanistic simulations, using data generated by domain-specific simulators to train flexible neural networks. In epidemiology, this means generating synthetic outbreaks from mechanistic disease models that capture processes such as transmission, progression, immunity, seasonality, and intervention effects, then training models on these simulated trajectories so they can forecast real-world outbreaks they have never encountered before. By grounding learning in simulated systems that encode known mechanisms—whether physical, biological, or social—SGNNs enable models to generalize to real-world settings where data are limited, noisy, or missing. Crucially, they retain interpretability by linking predictions back to the underlying mechanistic simulations that informed them [8].

We present Mantis, the first large-scale foundation model built on the SGNN paradigm. Building on early demonstrations of simulation-grounded forecasting [9], Mantis is trained entirely on mechanistic simulations without access to any real-world training data. It learns from over 400 million simulated days of outbreak dynamics spanning diverse pathogens, transmission routes (human-to-human, vector-borne, environmental), intervention strategies, immunity profiles, and surveillance artifacts such as underreporting and delays. These simulations encode core epidemiological mechanisms, allowing Mantis to internalize generalizable contagion dynamics rather than extrapolating from historical trends. Unlike traditional models, Mantis requires no disease-specific tuning or retraining, yet it produces accurate probabilistic forecasts out-of-the-box across diseases, geographies, and targets (Figure 1).

We evaluate Mantis against 39 models, across forecasting tasks spanning six real-world diseases: seasonal influenza, early COVID-19, dengue, hepatitis B, smallpox, and scarlet fever. These evaluations cover multiple transmission modes, outbreak phases, surveillance systems, and historical eras. In every comparison we tested, including those against published, expert-tuned models and CDC Forecast Hub models, Mantis outperformed all baselines. At 8-week horizons, Mantis achieved lower relative error than the CDC’s ensemble of COVID-19 forecasts at 4 weeks, despite using no COVID-specific data or covariates in training.

Together, these capabilities establish Mantis as a general-purpose, interpretable forecasting system ready for real-world use and offering a scalable new blueprint for modeling in data-scarce or rapidly evolving settings.

To support deployment, we release Mantis as an open-source repository. Users can generate forecasts from a single historical time series without any machine learning expertise.<sup>1</sup>

## Results

We assessed Mantis’s forecasting accuracy across a diverse benchmark suite of real-world tasks spanning six diseases: seasonal influenza, early COVID-19 [10], dengue [11], hepatitis B [12], smallpox [13], and scarlet fever [14]. For each task, we benchmarked Mantis against expert-tuned statistical and machine learning models, including published baselines and submissions to the CDC COVID-19 Forecast Hub [4] (see Methods).

Despite being trained entirely on synthetic data, Mantis consistently delivered state-of-the-art performance across all benchmarks we tested. Beyond raw accuracy, it enables reliable long-range forecasts up to 8 weeks ahead, generalizes out-of-the-box to novel diseases and epidemiological regimes, and provides mechanistic interpretability through back-to-simulation attribution.

---

<sup>1</sup>[github.com/carsondudley1/Mantis](https://github.com/carsondudley1/Mantis): Pretrained models, example data, and an interactive forecasting demo are available.

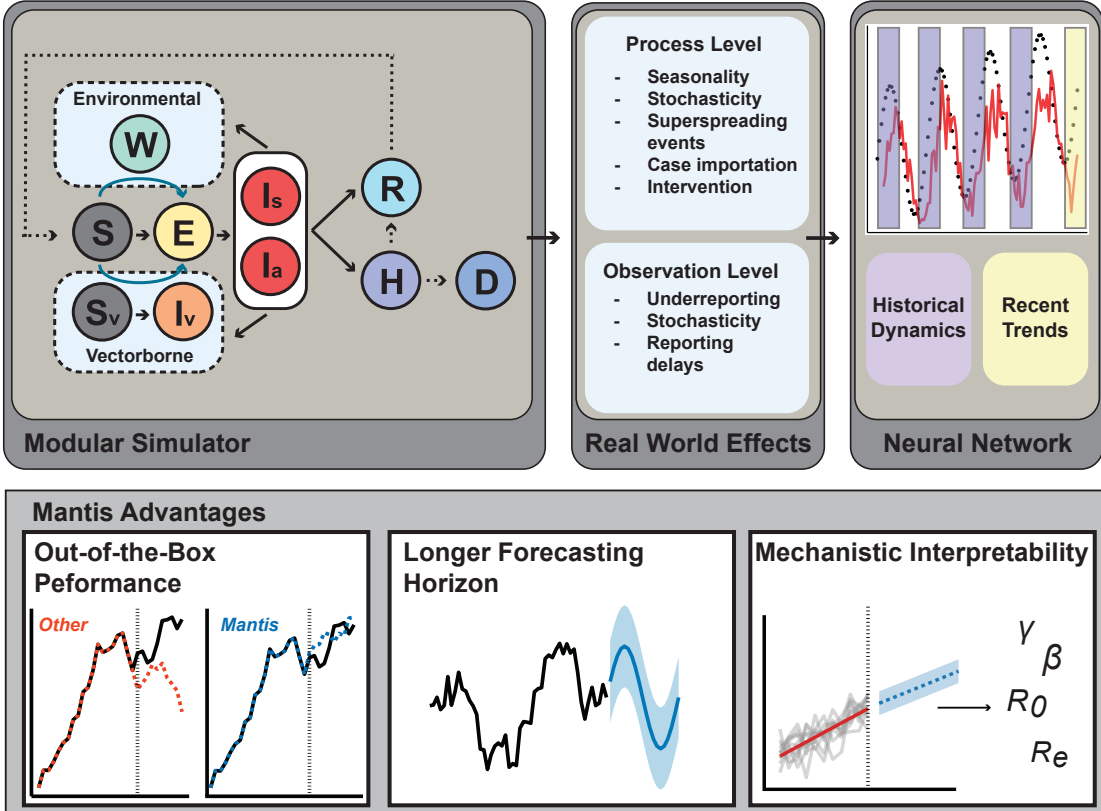


Figure 1: **Conceptual overview of Mantis.** Mantis is a simulation-grounded foundation model trained entirely on synthetic outbreaks generated by mechanistic epidemiological models. The training pipeline begins with a modular simulator that encodes diverse outbreak mechanisms, including multiple transmission modes (human-to-human, vectorborne, environmental), progression dynamics, intervention strategies, and population structures. These simulations are then passed through an observation model that incorporates real-world surveillance effects such as underreporting, stochasticity, and reporting delays. Trained on over 400 million simulated days, Mantis forecasts directly from real-world time series at inference time. Key advantages include accurate out-of-the-box performance, long-range forecasting capability, and mechanistic interpretability via back-to-simulation attribution.

## Mantis Achieves State-of-the-Art Accuracy Across Diseases and Tasks

For each disease, we evaluated performance across multiple spatial and temporal resolutions, including U.S. states and finer sub-state geographies, and at both the standard 4-week horizon [4] and a longer 8-week horizon. We compare Mantis against a range of published and re-implemented models, including top submissions to the CDC COVID-19 Forecast Hub, statistical baselines (naïve persistence and exponential smoothing), Chronos, a state-of-the-art time-series foundation model [15], and expert-tuned forecasting models previously developed for influenza.

Mantis outperformed every baseline across all diseases and tasks we tested (Figure 2a). This includes beating the CDC’s COVID-19 Forecast Hub ensemble, which combines dozens of expert-tuned models, even during volatile early-pandemic dynamics. We report forecasting improvement as the percent reduction in mean absolute error relative to the competing model for each task.

Example forecast trajectories illustrate Mantis’s ability to match the timing and magnitude of real-world outbreaks with high fidelity (Figure 3). Forecasts include uncertainty intervals derived from the model’s predicted quantiles, enabling direct use in probabilistic planning. Additional forecasts of both real disease data and simulated Mantis training data can be found in the supplement.

Because Mantis is trained entirely on mechanistic simulations rather than historical observations, it requires no model fitting or fine-tuning for new targets. This enables true out-of-the-box deployment—an advantage over historically trained models that require task-specific data and manual calibration before producing reliable forecasts.

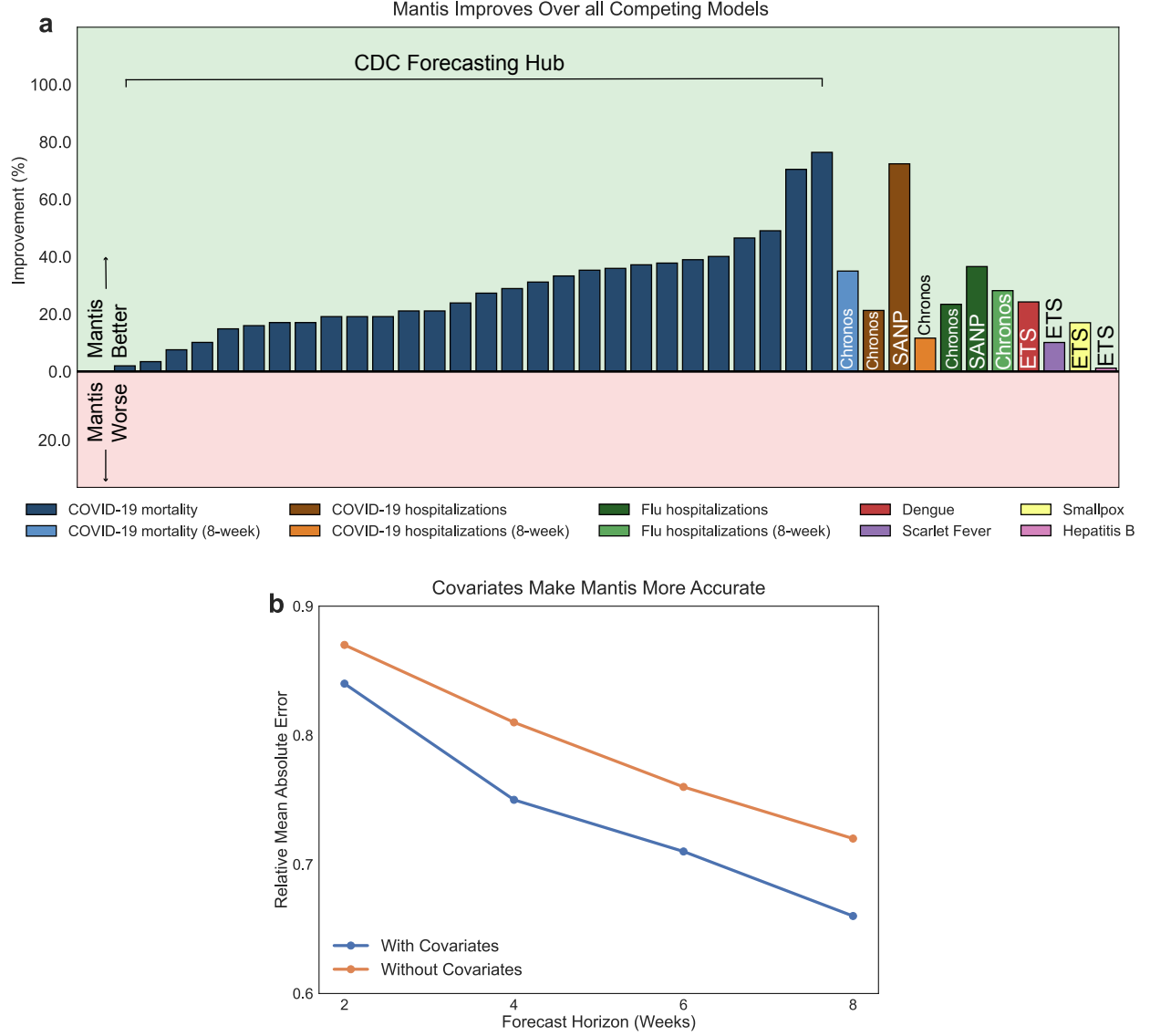


**Figure 2: Mantis Delivers Strong and Consistent Forecasting Performance.** (a) Mantis outperforms all baseline models across 39 forecasting tasks, including the top-ranked CDC COVID-19 Forecast Hub ensemble. Bars represent percent improvement in absolute error relative to the best competing model, stratified by disease and task. The abbreviation SANP means same architecture as Mantis, no pretraining. ETS models are exponential smoothing models. (b) Including contextual covariates (e.g., using cases to predict hospitalizations) consistently improves Mantis’s accuracy across all forecast horizons, highlighting the model’s ability to integrate heterogeneous inputs to enhance generalization.

## Covariate-Aware Mantis Improves Forecast Accuracy Across Horizons

We evaluated two variants of Mantis to assess the impact of auxiliary input information on forecasting performance: a covariate-free version, which receives only the time series to be forecast (e.g., deaths), and

a covariate-aware version, which also receives related signals such as cases and hospitalizations. This design mirrors real-world forecasting settings, where models may have access to upstream indicators with predictive value. (See Methods for training details for each model.)

For example, when forecasting COVID-19 deaths, the covariate-aware Mantis version receives both historical deaths and upstream case data, while the covariate-free version sees only the death time series. Both models use identical architecture and training data; the only difference is the presence or absence of additional input channels.

Across forecast horizons (2, 4, 6, and 8 weeks), the covariate-aware version consistently outperformed its covariate-free counterpart (Figure 2b), achieving lower mean absolute error across diseases and targets. These improvements were particularly pronounced at longer horizons, where upstream indicators (e.g., cases leading to hospitalizations, then deaths) provide early signals that improve downstream predictions.

These results highlight the benefit of incorporating complementary epidemiological signals when available and demonstrate that Mantis can flexibly leverage additional information without retraining. In data-rich settings, covariate-aware forecasts yield improved performance; in low-data contexts, the covariate-free version retains strong out-of-the-box accuracy, making both variants useful in practice depending on context and data availability.

## Mantis Enables Accurate Forecasts at Long Horizons

We evaluated Mantis’s long-range forecasting performance at an 8-week horizon across the same benchmark tasks and baselines described above. Mantis consistently achieved the lowest relative MAE across all diseases and targets tested, demonstrating its ability to extrapolate epidemiological dynamics further into the future than prior models. At the 8-week horizon, Mantis achieved lower relative error than all models in the CDC Forecast Hub at 4 weeks, and lower raw error than the median 4-week error of Forecast Hub models, demonstrating long-range accuracy that exceeds the short-term limits of existing expert-tuned systems.

Visual examples of 8-week forecasts show that Mantis captures outbreak peaks, rebounds, and multi-wave dynamics with high fidelity (Figure 3). Prediction intervals widen appropriately with time, maintaining calibrated uncertainty that reflects true forecast difficulty (for calibration results, see appendix D.1).

This capability is not enabled by manual tuning or disease-specific details, but by scale: Mantis learns from millions of simulated outbreak trajectories, encompassing diverse transmission patterns and intervention regimes. Unlike historically trained models, which rely on narrow slices of observed data, simulation-trained models like Mantis can internalize general patterns that support long-range prediction.

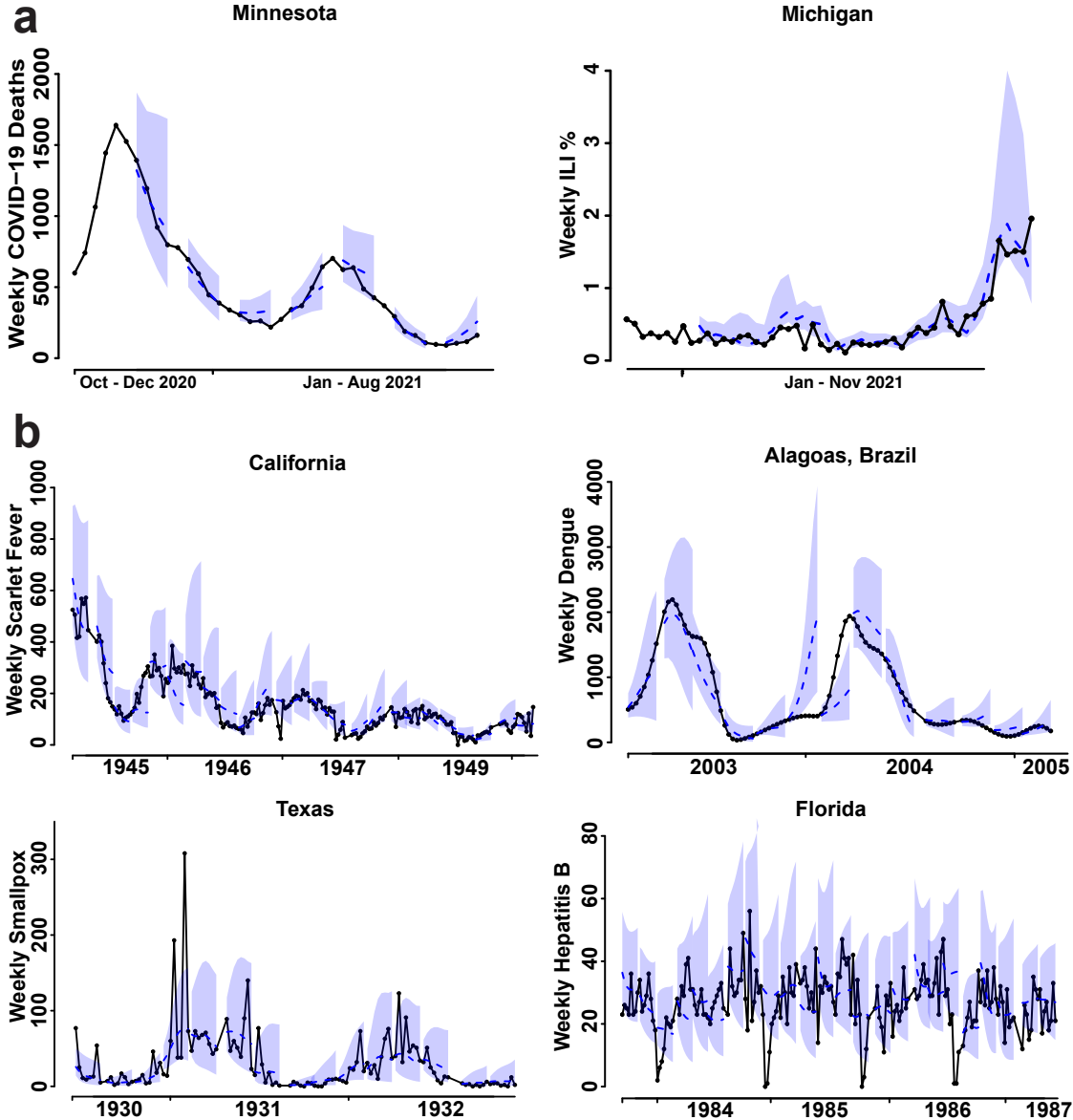


**Figure 3: Mantis Produces Accurate and Generalizable Forecasts Across Diseases and Geographies.** (a) Four-week-ahead forecasts (blue dashed line and shaded 90% CI) compared to observed outcomes (black) for COVID-19 mortality in Minnesota and influenza-like illness (ILI) in Michigan. In the latter, Mantis demonstrates its foundation model capacity by accurately forecasting syndromic inputs despite never being trained with syndromic data. (b) Eight-week-ahead forecasts for four historical outbreaks, highlighting Mantis’s ability to generalize across time, space, and transmission mode. In Alagoas, Brazil, Mantis forecasts the 2004 dengue surge prematurely, highlighting a failure in temporal calibration due to the absence of covariates, but still estimates the peak height with remarkable accuracy despite being 18 weeks early. Forecasts for hepatitis B in Florida—a chronic, bloodborne disease type absent from Mantis’s training set—further demonstrate its capacity to generalize to out-of-distribution disease profiles while maintaining forecast stability and accuracy.

### Mantis as a Foundation Model: Generalizing to New Mechanisms and Inputs

We next demonstrate Mantis’s out-of-the-box forecasting capacity across both held-out transmission mechanisms and new input data modalities.

First, we evaluated Mantis on diseases governed by transmission and progression mechanisms never represented in training simulations. For example, hepatitis B exhibits bloodborne transmission and chronic infection dynamics that are markedly different from the acute, self-limiting outbreaks used in pretraining. The Mantis training set included no models without recovery—all simulated diseases eventually transition out of the infectious state—and the longest average infectious period is just 10 days. In contrast, hepatitis B infection can persist for years. Despite this severe mismatch, Mantis outperformed statistical baselines trained directly on historical hepatitis B data (Fig. 3b, bottom right). These results demonstrate that Mantis can generalize across fundamental mechanistic boundaries—not just to new pathogens, but to qualitatively different epidemic regimes, such as chronic persistence versus outbreak spread.

Next, we tested Mantis’s ability to generalize across data modalities. Although trained using cases, hospitalizations, and deaths, Mantis can incorporate new input types at inference time. We show that a Mantis model trained without ever seeing syndromic surveillance data (percent of outpatient visits that were for influenza-like illness) can still accurately forecast these syndromic indicators (Fig. 3a, right). This capability is especially valuable in settings where conventional case counts may be missing or delayed, but syndromic indicators are available in near real-time.

In all settings we evaluated, Mantis outperforms comparison models trained directly on the task-specific data (Figure 2a). This level of generalization, across diseases, mechanisms, and modalities, underscores Mantis’s capacity as a true foundation model, and the advantages of scale afforded by simulation data. Rather than relying on domain-specific tuning, Mantis captures structural features of contagion that transfer across contexts, enabling immediate deployment in settings where other models would require retraining, expert tuning, or disease-specific data collection. Its ability to internalize general principles of transmission, rather than memorize specific patterns, makes it uniquely suited for forecasting in low-data and low-resource settings.

## Mantis Provides Mechanistic Interpretability via Back-to-Simulation Attribution

Forecast accuracy alone is not sufficient in high-stakes public health settings. Decision-makers must be able to understand and act on model outputs, especially when choosing between interventions with different risk profiles. To support this, Mantis leverages back-to-simulation attribution (back2sim) [8], a form of mechanistic interpretability that identifies the underlying dynamics the model believes are driving a forecast.

This approach offers a different kind of explanation than post-hoc methods like SHAP or LIME [16, 17]. While those methods can assign importance scores to input features—telling you which data points were influential—they often fail to explain why in a way that is meaningful for scientific or policy decisions. Back-to-simulation attribution answers the central question: what mechanisms does model think are driving this outbreak?

The attribution process works by comparing a real-world outbreak to the library of scenarios Mantis was trained on. The procedure consists of the following steps:

1. First, an input time series (e.g., observed COVID-19 mortality) is processed by Mantis to create an internal summary of its key dynamic features.
2. This summary is then used to search the training dataset and identify the simulated outbreaks that are the most similar in character.
3. Critically, the model is trained to look beyond superficial resemblances in the data. The retrieved simulations are therefore not simply those with similar-looking curves, but rather those that Mantis has learned are driven by analogous underlying processes (e.g., similar transmission dynamics or immunity profiles).
4. Finally, the known, ground-truth parameters of this retrieved set of simulations are aggregated to construct a quantitative, mechanism-level explanation for the forecast.

This procedure reveals the model’s mechanistic belief about what is driving the observed data, offering a transparent, domain-aligned interpretation of its forecast.

We visualize the mechanistic beliefs inferred by Mantis using a held-out simulated trajectory for which the true latent parameters are known, allowing direct validation of back-to-simulation attribution (Fig. 4). In

panel a, we show that the top-attributed simulations (gray lines) not only match the historical trajectory but also align closely with Mantis's forecast, indicating that attribution selects plausible trajectories consistent with both past and projected dynamics. Panel b demonstrates that the parameters associated with these retrieved simulations track the ground-truth values across epidemic waves for key latent variables, including asymptomatic probability, case hospitalization rate, and hospitalization fatality rate. These results show that Mantis accurately recovers dynamic changes in underlying drivers. Panel c compares the attributed parameter distributions (blue) to the full simulation prior (gray), revealing sharp concentration around Mantis's mechanistic beliefs and filtering out implausible settings. Finally, panel d confirms that attributed parameters cluster significantly closer to the true generative parameters than random samples from the prior, validating the precision and informativeness of Mantis's internal representations. Together, these results demonstrate that Mantis not only forecasts accurately, but also provides interpretable, mechanism-level hypotheses about what is driving epidemic dynamics.

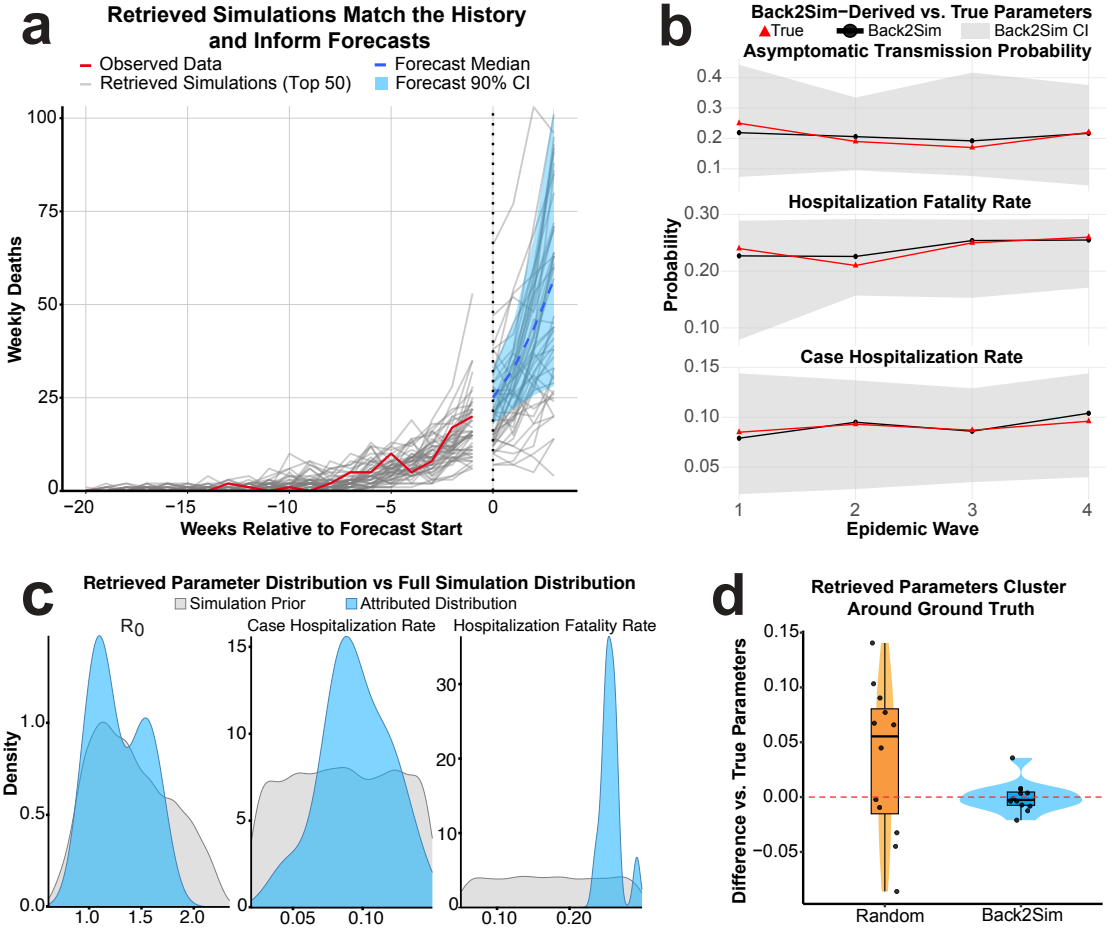


**Figure 4: Mechanistic Interpretability via Back-to-Simulation Attribution.** (a) Top-attributed simulations (gray) closely match the observed trajectory (red) and inform the forecast median and 90% confidence interval (blue), demonstrating temporal consistency and mechanistic plausibility. (b) Retrieved parameter estimates (black lines with 90% CI) for key latent variables—including asymptomatic transmission probability, hospitalization fatality rate, and case hospitalization rate—track true parameter values (red triangles) across epidemic waves, confirming the accuracy of back-to-simulation attribution. (c) Kernel density estimates of retrieved parameter distributions (blue) show strong sharpening relative to the simulation prior (gray), indicating Mantis's ability to concentrate mechanistic belief around plausible drivers of observed dynamics. (d) Retrieved parameters cluster significantly closer to ground truth than randomly selected simulations from the prior, confirming the informativeness and specificity of attribution-based mechanistic explanations.

## Discussion

Mantis demonstrates that accurate, long-range, and mechanistically interpretable infectious disease forecasting can be achieved without access to real-world training data. By learning entirely from simulated outbreaks, Mantis delivers strong performance across diverse real-world forecasting tasks and offers mechanistic explanations of its predictions through back-to-simulation attribution. These capabilities position Mantis as a practical and general-purpose tool for public health use, especially in low-resource or emerging outbreak settings where data may be limited or delayed. Because Mantis can generate forecasts with only a short initial observation window—as little as four weeks—it enables early situational awareness when conventional models are still inoperable.

While traditional forecasting models trained on historical data have been foundational for many operational systems, they often rely on disease-specific tuning and large volumes of real-world training data. Mantis departs from this paradigm: it consistently outperforms statistical, machine learning, and expert-tuned baselines across 39 real-world forecasting tasks, despite being trained on simulations alone. By proactively learning from mechanistic priors, Mantis supports plug-and-play forecasting in settings where retraining is infeasible and rapid response is essential.

The implications extend beyond public health. Mantis reflects an emerging shift toward simulation-supervised machine learning in scientific domains, where mechanistic models encode prior knowledge, and neural networks learn to generalize from them [8, 9]. This paradigm enables flexible, high-performance models that retain interpretability and domain alignment. Back-to-simulation attribution, in particular, provides a new form of interpretability tailored for science. Rather than explaining forecasts with abstract model internals, Mantis identifies which mechanistic regimes best explain the data. These attributions serve as hypotheses: falsifiable, domain-aligned, and directly actionable by public health decision-makers. This brings black-box forecasting closer to scientific reasoning—and enables the use of models not just for prediction, but for understanding.

While Mantis shows broad generalization, several limitations merit consideration. As shown in [8], the model’s performance depends on the diversity and realism of training simulations, though we demonstrate generalization beyond the specific regimes directly simulated during training. Additionally, Mantis inherits any systematic biases present in the underlying mechanistic models used for training. Another limitation concerns interpretability: back-to-simulation attribution currently operates by identifying training simulations most similar to the input trajectory, and thus can only attribute to mechanisms represented in the training data. While Mantis can accurately forecast dynamics outside the training distribution, its explanations are constrained by the set of simulated mechanisms available for comparison. Expanding the breadth of simulations used specifically for attribution may enable mechanistic explanations even in out-of-distribution scenarios, since Mantis could still forecast effectively in those situations. Future work should explore active learning approaches to identify and fill critical simulation gaps, and develop methods to detect when real-world dynamics fall outside reliable prediction boundaries.

Mantis illustrates a path forward for scientific forecasting systems that are interpretable, accurate, and rapidly deployable. Its out-of-the-box generalization makes it especially well-suited for early outbreak response, rural regions, and low- and middle-income countries—settings where traditional models often fail due to sparse or delayed data. By pairing simulation-based priors with flexible neural architectures, Mantis eliminates the longstanding trade-off between generalization and interpretability. It offers not just better predictions, but actionable, mechanism-level insights, making it a powerful foundation for future decision support systems in global public health.

## Methods

Here we provide a brief overview of the methods, with a complete description given in the Appendix.

### Training Mantis on Simulated Outbreaks

Mantis was trained entirely on synthetic outbreaks generated using mechanistic epidemiological models, following the framework developed in [8]. Simulations were based on compartmental disease models with

stochastic transitions and heterogeneous parameterizations, using three primary transmission routes: human-to-human respiratory illness models, vectorborne disease models (primarily inspired by arbovirus dynamics), and environmental transmission models (inspired by cholera and other environmentally transmitted pathogens). These models varied in transmission dynamics, disease severity, and intervention strategies to create a broad and diverse training distribution (see Appendix A for details). Each simulation generated daily time series of cases, hospitalizations, and deaths under a wide range of epidemic scenarios. In total, the training dataset included over 400 million days of data spanning thousands of parameter combinations.

## Neural Architecture and Training Procedure

Mantis uses a sequence-to-sequence neural network with convolutional and transformer-based components (Appendix B). The model takes an input context window of up to 112 weeks of observed time series and outputs probabilistic forecasts for multiple future targets (e.g., cases, hospitalizations, deaths). Forecasts are trained using a weighted quantile loss. We optimized the neural network using AdamW [18]. No real-world data are used during training.

## Evaluation on Real-World Forecasting Tasks

We evaluated Mantis across six diverse real-world infectious disease forecasting scenarios to assess generalization across pathogens, transmission modes, geographic scales, and historical periods (Appendix C). Our evaluation comprised two primary tasks and four additional challenges representing varying degrees of distribution shift from the model’s training data. Together, these datasets encompass over 39 forecasting tasks and more than 150,000 individual forecast evaluations, enabling rigorous assessment of Mantis’s capabilities across diverse epidemiological conditions, spatial resolutions, and outcome types. All Mantis evaluations were conducted in a strict zero-shot setting, with no fine-tuning or retraining on any evaluation data.

## Back-to-Simulation Attribution

To generate mechanistic explanations for its forecasts, Mantis performs back-to-simulation attribution [8]. During inference, the model encodes the observed input sequence into a learned latent representation. This encoding is used to retrieve the most similar training simulations in the latent space, which are then analyzed to summarize the likely underlying mechanisms driving the forecast. Attributions are visualized by aggregating simulator parameters across top-matched simulations.

## Author Contributions

CD led the study and developed the code and initial draft of the manuscript. CH and AS did the ablation studies and RM developed figure visualizations. CD, MCE, and RM all contributed substantial edits and revisions for the final manuscript.

## References

- [1] E. T. Lofgren, M. E. Halloran, C. M. Rivers, J. M. Drake, T. C. Porco, B. Lewis, W. Yang, A. Vespignani, J. Shaman, J. N. S. Eisenberg, M. C. Eisenberg, M. Marathe, S. V. Scarpino, K. A. Alexander, R. Meza, M. J. Ferrari, J. M. Hyman, L. A. Meyers, and S. Eubank. Mathematical models: A key tool for outbreak response. *Proceedings of the National Academy of Sciences*, 111(51):18095–18096, 2014.
- [2] Ashleigh R. Tuite, Joseph Tien, Marisa C. Eisenberg, et al. Cholera epidemic in haiti, 2010: Using a transmission model to explain spatial spread of disease and identify optimal control interventions. *Annals of Internal Medicine*, 154(9):593–601, 2011. [Epub 3 May 2011].
- [3] Jeremy P. D’Silva and Marisa C. Eisenberg. Modeling spatial invasion of ebola in west africa. *Journal of Theoretical Biology*, 428:65–75, September 2017. Published in final edited form: J Theor Biol. 2017 September 07; 428: 65–75.

[4] Estee Y. Cramer, Evan L. Ray, Velma K. Lopez, Johannes Bracher, Andrea Brennen, Alvaro J. Castro Rivadeneira, Aaron Gerdling, Tilmann Gneiting, Katie H. House, Yuxin Huang, Dasuni Jayawardena, Abdul H. Kanji, Ayush Khandelwal, Khoa Le, Anja Mühlemann, Jarad Niemi, Apurv Shah, Ariane Stark, Yijin Wang, Nutcha Wattanachit, Martha W. Zorn, Youyang Gu, Sansiddh Jain, Nayana Ban-nur, Ayush Deva, Mihir Kulkarni, Srujana Merugu, Alpan Raval, Siddhant Shingi, Avtansh Tiwari, Jerome White, Neil F. Abernethy, Spencer Woody, Maytal Dahan, Spencer Fox, Kelly Gaither, Michael Lachmann, Lauren Ancel Meyers, James G. Scott, Mauricio Tec, Ajitesh Srivastava, Glover E. George, Jeffrey C. Cegan, Ian D. Dettwiler, William P. England, Matthew W. Farthing, Robert H. Hunter, Brandon Lafferty, Igor Linkov, Michael L. Mayo, Matthew D. Parno, Michael A. Rowland, Benjamin D. Trump, Yanli Zhang-James, Samuel Chen, Stephen V. Faraone, Jonathan Hess, Christopher P. Morley, Asif Salekin, Dongliang Wang, Sabrina M. Corsetti, Thomas M. Baer, Marisa C. Eisenberg, Karl Falb, Yitao Huang, Emily T. Martin, Ella McCauley, Robert L. Myers, Tom Schwarz, Daniel Sheldon, Graham Casey Gibson, Rose Yu, Liyao Gao, Yian Ma, Dongxia Wu, Xifeng Yan, Xiaoyong Jin, Yu-Xiang Wang, YangQuan Chen, Lihong Guo, Yanting Zhao, Quanquan Gu, Jinghui Chen, Lingxiao Wang, Pan Xu, Weitong Zhang, Difan Zou, Hannah Biegel, Joceline Lega, Steve McConnell, V. P. Nagraj, Stephanie L. Guertin, Christopher Hulme-Lowe, Stephen D. Turner, Yunfeng Shi, Xuegang Ban, Robert Walraven, Qi-Jun Hong, Stanley Kong, Axel van de Walle, James A. Turtle, Michal Ben-Nun, Steven Riley, Pete Riley, Ugur Koayluoglu, David DesRoches, Pedro Forli, Bruce Hamory, Christina Kyriakides, Helen Leis, John Milliken, Michael Moloney, James Morgan, Ninad Nirgudkar, Gokce Ozcan, Noah Pi-wonka, Matt Ravi, Chris Schrader, Elizabeth Shakhnovich, Daniel Siegel, Ryan Spatz, Chris Stiefeling, Barrie Wilkinson, Alexander Wong, Sean Cavany, Guido España, Sean Moore, Rachel Oidtman, Alex Perkins, David Kraus, Andrea Kraus, Zhifeng Gao, Jiang Bian, Wei Cao, Juan Lavista Ferres, Chaozhuo Li, Tie-Yan Liu, Xing Xie, Shun Zhang, Shun Zheng, Alessandro Vespiagnani, Matteo Chinazzi, Jessica T. Davis, Kumpeng Mu, Ana Pastore y Piontti, Xinyue Xiong, Andrew Zheng, Jackie Baek, Vivek Farias, Andreea Georgescu, Retsef Levi, Deeksha Sinha, Joshua Wilde, Georgia Perakis, Mohammed Amine Bennouna, David Nze-Ndong, Divya Singhvi, Ioannis Spantidakis, Leann Thayaparan, Asterios Tsiorvas, Arnab Sarker, Ali Jadbabaie, Devavrat Shah, Nicolas Della Penna, Leo A. Celi, Saketh Sundar, Russ Wolfinger, Dave Osthuis, Lauren Castro, Geoffrey Fairchild, Isaac Michaud, Dean Karlen, Matt Kinsey, Luke C. Mullany, Kaitlin Rainwater-Lovett, Lauren Shin, Katharine Tallaksen, Shelby Wilson, Elizabeth C. Lee, Juan Dent, Kyra H. Grantz, Alison L. Hill, Joshua Kaminsky, Kathryn Kaminsky, Lindsay T. Keegan, Stephen A. Lauer, Joseph C. Lemaitre, Justin Lessler, Hannah R. Meredith, Javier Perez-Saez, Sam Shah, Claire P. Smith, Shaun A. Truelove, Josh Wills, Maximilian Marshall, Lauren Gardner, Kristen Nixon, John C. Burant, Lily Wang, Lei Gao, Zhiling Gu, Myungjin Kim, Xinyi Li, Guannan Wang, Yueying Wang, Shan Yu, Robert C. Reiner, Ryan Barber, Emmanuela Gakidou, Simon I. Hay, Steve Lim, Chris Murray, David Pigott, Heidi L. Gurung, Prasith Baccam, Steven A. Stage, Bradley T. Suchoski, B. Aditya Prakash, Bijaya Adhikari, Jiaming Cui, Alexander Rodríguez, Anika Tabassum, Jiajia Xie, Pinar Keskinocak, John Asplund, Arden Baxter, Buse Eylul Oruc, Nicoleta Serban, Sercan O. Arik, Mike Dusenberry, Arkady Epshteyn, Elli Kanal, Long T. Le, Chun-Liang Li, Tomas Pfister, Dario Sava, Rajarishi Sinha, Thomas Tsai, Nate Yoder, Jinsung Yoon, Leyou Zhang, Sam Abbott, Nikos I. Bosse, Sebastian Funk, Joel Hellewell, Sophie R. Meakin, Katharine Sherratt, Mingyuan Zhou, Rahi Kalantari, Teresa K. Yamana, Sen Pei, Jeffrey Shaman, Michael L. Li, Dimitris Bertsimas, Omar Skali Lami, Saksham Soni, Hamza Tazi Bouardi, Turgay Ayer, Madeline Ade, Jagpreet Chhatwal, Ozden O. Dalgic, Mary A. Ladd, Benjamin P. Linas, Peter Mueller, Jade Xiao, Yuanjia Wang, Qinxia Wang, Shanghong Xie, Donglin Zeng, Alden Green, Jacob Bien, Logan Brooks, Addison J. Hu, Maria Jahja, Daniel McDonald, Balasubramanian Narasimhan, Collin Politsch, Samyak Rajanala, Aaron Rumack, Noah Simon, Ryan J. Tibshirani, Rob Tibshirani, Valerie Ventura, Larry Wasserman, Eamon B. O'Dea, John M. Drake, Robert Pagano, Quoc T. Tran, Lam Si Tung Ho, Huong Huynh, Jo W. Walker, Rachel B. Slayton, Michael A. Johansson, Matthew Biggerstaff, and Nicholas G. Reich. Evaluation of individual and ensemble probabilistic forecasts of covid-19 mortality in the united states. *Proceedings of the National Academy of Sciences*, 119(15):e2113561119, 2022.

[5] Alexander Rodriguez, Anika Tabassum, Jiaming Cui, Jiajia Xie, Javen Ho, Pulak Agarwal, Bijaya Adhikari, and Aditya Prakash. Deepcovid: An operational deep learning-driven framework for explainable real-time covid-19 forecasting. In *Proceedings of the AAAI Conference on Artificial Intelligence*,

volume 35, 2021.

- [6] Dongxia Wu, Liyao Gao, Xinyue Xiong, Matteo Chinazzi, Alessandro Vespignani, Yi-An Ma, and Rose Yu. Deepgleam: A hybrid mechanistic and deep learning model for covid-19 forecasting, 2021.
- [7] Sebastian Funk, Anton Camacho, Adam J Kucharski, Rachel Lowe, Rosalind M Eggo, and W John Edmunds. Assessing the performance of real-time epidemic forecasts: A case study of ebola in the western area region of sierra leone, 2014–15. *PLOS Computational Biology*, 15(2):e1006785, 2019.
- [8] Carson Dudley, Reiden Magdaleno, Christopher Harding, and Marisa Eisenberg. Simulation as supervision: Mechanistic pretraining for scientific discovery, 2025.
- [9] Lijing Wang, Jiangzhuo Chen, and Madhav Marathe. Defsi: Deep learning based epidemic forecasting with synthetic information. In *Proceedings of the AAAI Conference on Artificial Intelligence*, volume 33, 2019.
- [10] CDC COVID-19 Response. Weekly united states covid-19 cases and deaths by state - archived. <https://data.cdc.gov/Case-Surveillance/Weekly-United-States-COVID-19-Cases-and-Deaths-by-/pwn4-m3yp>, 2025. Centers for Disease Control and Prevention. Dataset last updated: June 1, 2023. Metadata last updated: February 23, 2025. Temporal coverage: 2020-01-22 to 2023-05-10.
- [11] Willem Van Panhuis, Abigail Cross, and Donald Burke. Counts of dengue without warning signs reported in brazil: 1980–2005 (2.0) [data set]. <https://doi.org/10.25337/T7/ptycho.v2.0/BR.722862003>, 2018. Project Tycho.
- [12] Willem Van Panhuis, Abigail Cross, and Donald Burke. Counts of viral hepatitis type b reported in united states of america: 1951–2007 (2.0) [data set]. <https://doi.org/10.25337/T7/ptycho.v2.0/US.66071002>, 2018. Project Tycho.
- [13] Willem Van Panhuis, Abigail Cross, and Donald Burke. Counts of smallpox reported in united states of america: 1888–1952 (2.0) [data set]. <https://doi.org/10.25337/T7/ptycho.v2.0/US.67924001>, 2018. Project Tycho.
- [14] Willem Van Panhuis, Abigail Cross, and Donald Burke. Counts of scarlet fever reported in united states of america: 1888–1969 (2.0) [data set]. <https://doi.org/10.25337/T7/ptycho.v2.0/US.30242009>, 2018. Project Tycho.
- [15] Abdul Fatir Ansari, Lorenzo Stella, Caner Turkmen, Xiyuan Zhang, Pedro Mercado, Huibin Shen, Oleksandr Shchur, Syama Sundar Rangapuram, Sebastian Pineda Arango, Shubham Kapoor, Jasper Zschiegner, Danielle C. Maddix, Hao Wang, Michael W. Mahoney, Kari Torkkola, Andrew Gordon Wilson, Michael Bohlke-Schneider, and Yuyang Wang. Chronos: Transformer-based language models for time-series forecasting, 2024.
- [16] Scott Lundberg and Su-In Lee. A unified approach to interpreting model predictions, 2017.
- [17] Marco Tulio Ribeiro, Sameer Singh, and Carlos Guestrin. "why should i trust you?": Explaining the predictions of any classifier, 2016.
- [18] Ilya Loshchilov and Frank Hutter. Decoupled weight decay regularization, 2019.
- [19] Hualei Xin, Yu Li, Peng Wu, Zhili Li, Eric HY Lau, Ying Qin, Liping Wang, Benjamin J Cowling, Tim K Tsang, and Zhongjie Li. Estimating the latent period of coronavirus disease 2019 (covid-19). *Clinical Infectious Diseases*, 74(9):1678–1681, 2022.
- [20] Vincent Ka Chun Yan, Eric Yuk Fai Wan, Xuxiao Ye, Anna Hoi Ying Mok, Francisco Tsz Tsun Lai, Celine Sze Ling Chui, Xue Li, Carlos King Ho Wong, Philip Hei Li, Tiantian Ma, Simon Qin, Chak Sing Lau, Ian Chi Kei Wong, and Esther Wai Yin Chan. Waning effectiveness against covid-19-related hospitalization, severe complications, and mortality with two to three doses of coronavac and bnt162b2: a case-control study. *Emerging Microbes & Infections*, 12:2209201, 2023.

[21] Michigan State Police, Emergency Management & Homeland Security Division. Regional map: Emergency management & homeland security division, michigan state police, October 2024. Last updated October 1, 2024.

[22] David C. Farrow, Logan C. Brooks, Aaron Rumack, Ryan J. Tibshirani, and Roni Rosenfeld. Delphi epidata api. <https://github.com/cmu-delphi/delphi-epidata>, 2015. Carnegie Mellon University, Delphi Research Group.

# Appendices

## A Training Data

### Human-to-Human Transmission Simulator

The human-to-human transmission simulator implements a stochastic compartmental model that captures the complex dynamics of respiratory pathogens spreading through direct contact. This simulator generates diverse outbreak scenarios by randomly sampling from wide parameter ranges, producing synthetic epidemics that span the spectrum from influenza-like seasonal patterns to COVID-like pandemic dynamics.

#### Model Structure

**Compartmental Framework** The core model follows a flexible SEAIR structure (Susceptible, Exposed, Asymptomatic, Infectious, Recovered) with optional latent periods, asymptomatic transmission, and waning immunity. These structural features are included probabilistically during simulation generation, allowing Mantis to learn from a wide range of outbreak regimes, including both acute and chronic infections, and both simple and complex transmission pathways. For example, in some simulations, all exposed individuals transition directly to the infectious state (i.e., no latent period); in others, asymptomatic infections are excluded, reflecting diseases without subclinical spread.

When fully enabled, the population is divided into five compartments:

$$\frac{dS}{dt} = -\lambda S + \omega R + bN - dS \quad (1)$$

$$\frac{dE}{dt} = \lambda S - \sigma E - dE \quad (2)$$

$$\frac{dA}{dt} = p_a \sigma E - \gamma_a A - dA \quad (3)$$

$$\frac{dI}{dt} = (1 - p_a) \sigma E - \gamma I - dI \quad (4)$$

$$\frac{dR}{dt} = \gamma_a A + \gamma I - \omega R - dR \quad (5)$$

where:

- $S$ : Susceptible individuals
- $E$ : Exposed (latent) individuals
- $A$ : Asymptomatic infectious individuals
- $I$ : Symptomatic infectious individuals
- $R$ : Recovered/immune individuals
- $N = S + E + A + I + R$ : Total population

**Force of Infection** The force of infection  $\lambda$  incorporates contributions from both symptomatic and asymptomatic individuals:

$$\lambda(t) = \beta(t) \cdot s(t) \cdot \left( \frac{I + \alpha A}{N} \right) \cdot m(t) \quad (6)$$

where:

- $\beta(t)$ : Time-varying transmission rate (allows for multiple waves)
- $s(t)$ : Seasonal forcing factor
- $\alpha$ : Relative transmissibility of asymptomatic individuals
- $m(t)$ : Super-spreading multiplier

**Model Parameters** The model includes the following epidemiological parameters:

- $\sigma$ : Progression rate from exposed to infectious ( $1/\sigma$  = latent period)
- $\gamma$ : Recovery rate for symptomatic individuals ( $1/\gamma$  = infectious period)
- $\gamma_a$ : Recovery rate for asymptomatic individuals
- $\omega$ : Waning immunity rate ( $1/\omega$  = duration of immunity)
- $p_a$ : Probability of asymptomatic infection
- $b$ : Birth rate
- $d$ : Death rate

### Stochastic Implementation

The continuous-time model is implemented as a discrete-time stochastic process using daily time steps. At each time step  $t$ , transitions between compartments are drawn from binomial distributions (equivalent to tau-leaping with large tau, but we found that it improved performance):

$$\text{New exposures} \sim \text{Binomial}(S_t, 1 - e^{-\lambda_t}) \quad (7)$$

$$E \rightarrow I/A \text{ transitions} \sim \text{Binomial}(E_t, 1 - e^{-\sigma}) \quad (8)$$

$$\text{Recoveries from I} \sim \text{Binomial}(I_t, 1 - e^{-\gamma}) \quad (9)$$

$$\text{Recoveries from A} \sim \text{Binomial}(A_t, 1 - e^{-\gamma_a}) \quad (10)$$

$$\text{Waning immunity} \sim \text{Binomial}(R_t, 1 - e^{-\omega}) \quad (11)$$

Among newly infectious individuals, the split between asymptomatic and symptomatic follows:

$$\text{New asymptomatic} \sim \text{Binomial}(\text{New infectious}, p_a) \quad (12)$$

### Multi-Wave Dynamics

To capture realistic outbreak patterns with multiple waves, the transmission rate  $\beta(t)$  is implemented as a piecewise constant function:

$$\beta(t) = \beta_i \quad \text{for } t \in [t_{i-1}, t_i) \quad (13)$$

where  $t_0, t_1, \dots, t_k$  are randomly chosen wave change points and  $\beta_1, \beta_2, \dots, \beta_k$  are independently sampled transmission rates. The number of wave changes is drawn from a discrete uniform distribution, and change points are sampled uniformly within the simulation period.

## Seasonal Forcing

Seasonal transmission patterns are modeled using multiple harmonic components:

$$s(t) = 1 + \sum_{j=1}^{n_h} A_j \cos\left(\frac{2\pi(t - \phi_j + \delta_y)}{P_j}\right) + \epsilon_t \quad (14)$$

where:

- $n_h$ : Number of harmonic components (1-4)
- $A_j$ : Amplitude of harmonic  $j$
- $P_j$ : Period of harmonic  $j$  (365.0, 182.5, or 91.25 days)
- $\phi_j$ : Phase offset for harmonic  $j$
- $\delta_y$ : Annual peak jitter, sampled independently each year to slightly shift seasonal peaks and avoid perfectly periodic recurrence
- $\epsilon_t$ : Daily multiplicative noise  $\sim \mathcal{N}(1, 0.05^2)$

## Super-Spreading Events

Super-spreading is modeled through a stochastic multiplier applied to the force of infection. At each time step, a subset of infectious individuals becomes super-spreaders with probability  $p_{ss}$ . The transmission enhancement follows a Gamma distribution:

$$m(t) = \left(1 - \frac{n_{ss}}{n_I}\right) + \frac{n_{ss}}{n_I} \cdot M \quad (15)$$

where  $n_{ss} \sim \text{Binomial}(n_I, p_{ss})$  and  $M \sim \text{Gamma}(k_{ss}, \theta_{ss})$ .

## Intervention Policies

The simulator includes an optional universal intervention policy that modulates transmission based on case thresholds. The policy operates through a contact reduction factor applied to  $\beta(t)$ :

$$\beta_{eff}(t) = \beta(t) \cdot r_{contact}(t) \quad (16)$$

where  $r_{contact}(t) \in [0.2, 1.0]$  represents the intervention strength. The policy activates when daily cases exceed an on-threshold and deactivates after cases remain below an off-threshold for a specified duration.

## Endemic Dynamics

For simulations with endemic circulation, demographic processes are included:

$$\text{Births} \sim \text{Poisson}(b \cdot N) \quad (17)$$

$$\text{Deaths} \sim \text{Binomial}(X, \min(d, 1)) \quad \forall X \in \{S, E, A, I, R\} \quad (18)$$

$$\text{Importations} \sim \text{Poisson}(\iota) \quad (19)$$

New births enter the susceptible compartment, deaths occur proportionally across all compartments, and imported cases enter the exposed or infectious compartment.

## Observation Model

True epidemic dynamics are converted to observed case counts through a comprehensive noise injection pipeline that simulates real-world surveillance artifacts:

**Multiplicative Noise** Base case counts are perturbed with log-normal noise:

$$\hat{C}_t = C_t \cdot \epsilon_t, \quad \epsilon_t \sim \text{LogNormal}(0, \sigma_{mult}^2) \quad (20)$$

**Underreporting** Reporting rates evolve logically over time:

$$r_t = r_0 + (r_\infty - r_0) \cdot \frac{1}{1 + e^{-k(t-t_{mid})}} \quad (21)$$

Reported cases follow:  $\tilde{C}_t \sim \text{Binomial}(\hat{C}_t, r_t)$

**Reporting Delays** Cases are distributed across future days using inverse-weighted delay distributions:

$$P(\text{delay} = d) \propto \frac{\alpha}{d+1}, \quad d \in [0, D_{max}] \quad (22)$$

**Day-of-Week Effects** Reporting varies by weekday with multiplicative factors:

$$\tilde{C}'_t = \tilde{C}_t \cdot w(\text{day-of-week}(t)) \quad (23)$$

where  $w(\cdot)$  ranges from 0.4 (weekend) to 1.2 (Tuesday).

## Hospitalization and Death Generation

Secondary outcomes (hospitalizations and deaths) are derived from symptomatic cases using time-varying probabilities and delay distributions. For each wave segment  $i$ , hospitalization and death probabilities ( $p_{h,i}$  and  $p_{d,i}$ ) are independently sampled.

### Hospitalization Process

$$H_t = \sum_{\tau=0}^t \text{Binomial}(I_\tau, p_{h, \text{wave}(\tau)}) \cdot f_h(t - \tau) \quad (24)$$

$$f_h(d) \sim \text{Gamma}(k_h, \theta_h) \quad (25)$$

**Death Process** Deaths occur among hospitalized individuals with additional delays:

$$D_t = \sum_{\tau=0}^t \sum_{s=0}^{\tau} \text{Binomial}(H_{\tau,s}, p_{d, \text{wave}(s)}) \cdot f_d(t - \tau) \quad (26)$$

$$f_d(d) \sim \text{Gamma}(k_d, \theta_d) \quad (27)$$

where  $H_{\tau,s}$  represents hospitalizations on day  $\tau$  originating from infections on day  $s$ .

## Parameter Ranges

Table 1 summarizes all parameters and their sampling distributions used in the human-to-human transmission simulator. Parameters were chosen to be broadly consistent with respiratory pathogens.

Table 1: Human-to-Human Transmission Simulator Parameters

Parameter	Symbol	Range/Distribution	Units
<b>Population and Simulation</b>			
Population size	$N$	Log-uniform[50,000, 40,000,000]	individuals
Simulation days	$T$	2,000	days
<b>Core Transmission Parameters</b>			
Base transmission rate	$\beta$	Uniform[0.2, 0.235]	$\text{day}^{-1}$
Recovery rate	$\gamma$	Uniform[0.1, 0.33]	$\text{day}^{-1}$
Latent progression rate	$\sigma$	Uniform[0.2, 0.4] [19]	$\text{day}^{-1}$
Waning immunity rate	$\omega$	Uniform[0.001, 0.0075] [20]	$\text{day}^{-1}$
<b>Asymptomatic Dynamics</b>			
Asymptomatic probability	$p_a$	Beta(3, 7)	proportion
Asymp. transmissibility	$\alpha$	Beta(2, 5)	proportion
Has asymptomatic compartment	-	Bernoulli(0.5)	boolean
<b>Model Structure Options</b>			
Has latent period	-	Bernoulli(0.7)	boolean
Has waning immunity	-	Bernoulli(0.9)	boolean
<b>Multi-Wave Dynamics</b>			
Multiple waves enabled	-	Configurable (default: True)	boolean
Number of wave changes	-	Uniform[0, 4]	count
Wave change days	-	Uniform[50, 1800]	days
<b>Super-Spreading</b>			
Super-spreader probability	$p_{ss}$	Uniform[0.0005, 0.02]	proportion
Multiplier shape	$k_{ss}$	4.0	-
Multiplier scale	$\theta_{ss}$	1.5	-
<b>Seasonality</b>			
Use seasonality	-	Bernoulli(0.8)	boolean
Number of harmonics	$n_h$	Uniform[1, 4]	count
Harmonic amplitude	$A_j$	Base $\times$ Uniform[0.3, 1.0]	proportion
Base amplitude	-	Uniform[0.1, 0.5]	proportion
Phase offset	$\phi_j$	Uniform[0, 365] + Uniform[-60, 60]	days
Possible periods	$P_j$	Choice[365.0, 182.5, 91.25]	days
Daily noise std	$\sigma_\epsilon$	0.05	proportion
Annual peak jitter	$\delta_y$	Uniform[-30, 30]	days
<b>Endemic Demographics</b>			
Enable endemic	-	Bernoulli(0.8)	boolean
Birth rate	$b$	Uniform[0.00002, 0.00012]	$\text{day}^{-1}$
Death rate factor	-	Uniform[0.8, 1.3]	proportion
Importation rate	$\iota$	Exp(Uniform[ln(0.01), ln(0.5)])	$\text{day}^{-1}$
<b>Intervention Policy</b>			
Enable intervention	-	Bernoulli(0.25)	boolean
On threshold	-	$N \times \text{Uniform}[1e-5, 1e-3]$	cases/day
Off threshold	-	On threshold $\times$ Uniform[0, 1]	cases/day
Contact reduction	$r_{contact}$	Uniform[0.2, 0.6]	proportion
Trigger delay	-	Uniform[0, 21]	days

Continued on next page

**Table 1 – continued from previous page**

Parameter	Symbol	Range/Distribution	Units
Minimum duration	-	Uniform[14, 35]	days
Maximum duration	-	Choice[None, Uniform[60, 120]]	days
Consecutive off days	-	Uniform[1, 50]	days
<b>Observation Noise</b>			
Multiplicative noise std	$\sigma_{mult}$	0.1	log-scale
Overdispersion parameter	$r$	1200	-
<b>Reporting Effects</b>			
Apply reporting rate	-	Bernoulli(0.8)	boolean
Initial reporting rate	$r_0$	Uniform[0.05, 0.4]	proportion
Final reporting rate	$r_\infty$	Uniform[0.25, 0.85]	proportion
Days to max testing	-	Uniform[30, 365]	days
Logistic steepness	$k$	Uniform[4, 8]	-
Apply weekday effects	-	Bernoulli(0.8)	boolean
Monday factor	-	Normal(1.2, 0.15)	proportion
Tue-Thu factor	-	Normal(1.0, 0.1)	proportion
Friday factor	-	Normal(0.9, 0.12)	proportion
Saturday factor	-	Normal(0.6, 0.2)	proportion
Sunday factor	-	Normal(0.4, 0.2)	proportion
Apply lab noise	-	Bernoulli(0.8)	boolean
Lab batch size	-	Poisson(100)	samples
Bad batch rate	-	0.005	proportion
Bad batch accuracy	-	Uniform[0.7, 0.85]	proportion
Apply delays	-	Bernoulli(0.8)	boolean
Initial max delay	-	Uniform[7, 21]	days
Final max delay	-	Uniform[2, 7]	days
Initial alpha	$\alpha_0$	1.0	-
Final alpha	$\alpha_\infty$	4.0	-
<b>Hospitalization &amp; Death</b>			
Hospitalization probability	$p_{h,i}$	Uniform[0.02, 0.15] per wave	proportion
Death probability (of hosp.)	$p_{d,i}$	Uniform[0.05, 0.3] per wave	proportion
Hosp. delay shape	$k_h$	Uniform[2.0, 4.0]	-
Hosp. delay scale	$\theta_h$	Uniform[1.0, 3.0]	days
Death delay shape	$k_d$	Uniform[1.5, 2.5]	-
Death delay scale	$\theta_d$	Uniform[4.5, 8.5]	days

This comprehensive parameter space enables the generation of diverse outbreak scenarios spanning different pathogen characteristics, population contexts, surveillance qualities, and intervention regimes. Each simulation run samples independently from these distributions, creating a rich training corpus that captures the full spectrum of human-to-human transmission dynamics.

## Vector-Borne Transmission Simulator

The vector-borne transmission simulator implements a coupled host-vector compartmental model that captures the complex dynamics of diseases transmitted through arthropod vectors, such as dengue, Zika, chikungunya, and malaria. This simulator models the epidemiological dynamics within both human and vector populations, incorporating realistic vector ecology, seasonal patterns, and intervention strategies.

## Model Structure

**Coupled Host-Vector Framework** The model consists of two interacting population systems: humans and vectors (typically mosquitoes). The human population follows a SEAIR structure similar to the human-to-human model, while vectors follow a simpler SEI structure without recovery (as infected vectors typically remain infectious for life).

**Human Population Dynamics** The human compartments evolve according to:

$$\frac{dS_h}{dt} = -\lambda_h S_h + \omega R_h + b_h N_h - d_h S_h \quad (28)$$

$$\frac{dE_h}{dt} = \lambda_h S_h - \sigma_h E_h - d_h E_h \quad (29)$$

$$\frac{dA_h}{dt} = p_a \sigma_h E_h - \gamma_a A_h - d_h A_h \quad (30)$$

$$\frac{dI_h}{dt} = (1 - p_a) \sigma_h E_h - \gamma I_h - d_h I_h \quad (31)$$

$$\frac{dR_h}{dt} = \gamma_a A_h + \gamma I_h - \omega R_h - d_h R_h \quad (32)$$

**Vector Population Dynamics** The vector compartments evolve according to:

$$\frac{dS_v}{dt} = \mu_v N_v - \lambda_v S_v - \mu_v S_v \quad (33)$$

$$\frac{dE_v}{dt} = \lambda_v S_v - \sigma_v E_v - \mu_v E_v \quad (34)$$

$$\frac{dI_v}{dt} = \sigma_v E_v - \mu_v I_v \quad (35)$$

where  $N_v = S_v + E_v + I_v$  is the total vector population.

**Force of Infection** The transmission between humans and vectors occurs through biting interactions. The force of infection for humans (from infected vectors) is:

$$\lambda_h(t) = a \cdot b_h \cdot \frac{I_v}{N_v} \cdot \beta(t) \cdot s(t) \cdot f_{intervention}(t) \quad (36)$$

The force of infection for vectors (from infected humans) is:

$$\lambda_v(t) = a \cdot b_v \cdot \frac{I_h + \alpha A_h}{N_h} \cdot \beta(t) \cdot s(t) \cdot f_{intervention}(t) \quad (37)$$

where:

- $a$ : Biting rate (bites per vector per day)
- $b_h$ : Probability of transmission from vector to human per bite
- $b_v$ : Probability of transmission from human to vector per bite
- $\beta(t)$ : Time-varying transmission scaling factor
- $s(t)$ : Seasonal forcing function
- $f_{intervention}(t)$ : Intervention effectiveness factor
- $\alpha$ : Relative transmissibility of asymptomatic humans

## Stochastic Implementation

The continuous-time model is implemented as a discrete-time stochastic process. At each time step  $t$ , transitions are drawn from binomial distributions:

### Human Transitions

$$\text{New human exposures} \sim \text{Binomial}(S_h(t), 1 - e^{-\lambda_h(t)}) \quad (38)$$

$$E_h \rightarrow I_h/A_h \sim \text{Binomial}(E_h(t), 1 - e^{-\sigma_h}) \quad (39)$$

$$\text{Human recoveries from } I \sim \text{Binomial}(I_h(t), 1 - e^{-\gamma}) \quad (40)$$

$$\text{Human recoveries from } A \sim \text{Binomial}(A_h(t), 1 - e^{-\gamma_a}) \quad (41)$$

$$\text{Waning immunity} \sim \text{Binomial}(R_h(t), 1 - e^{-\omega}) \quad (42)$$

### Vector Transitions

$$\text{New vector exposures} \sim \text{Binomial}(S_v(t), 1 - e^{-\lambda_v(t)}) \quad (43)$$

$$E_v \rightarrow I_v \sim \text{Binomial}(E_v(t), 1 - e^{-\sigma_v}) \quad (44)$$

$$\text{Vector deaths from } S \sim \text{Binomial}(S_v(t), \mu_v) \quad (45)$$

$$\text{Vector deaths from } E \sim \text{Binomial}(E_v(t), \mu_v) \quad (46)$$

$$\text{Vector deaths from } I \sim \text{Binomial}(I_v(t), \mu_v) \quad (47)$$

$$\text{New vector births} \sim \text{Poisson}(\mu_v N_v(t)) \quad (48)$$

### Vector Population Dynamics

Vector populations exhibit distinct ecological patterns compared to human populations:

**Mortality and Reproduction** Vectors have high mortality rates ( $\mu_v$ ) with typical lifespans of 10-30 days. To maintain population equilibrium, new vectors are born at rate  $\mu_v N_v$ , entering the susceptible class.

**Seasonal Patterns** Vector abundance and activity are strongly seasonal, captured through enhanced seasonal forcing:

$$s(t) = 1.2 + \sum_{j=1}^{n_h} A_j \cos\left(\frac{2\pi(t - \phi_j + \delta_y)}{P_j}\right) + \epsilon_t \quad (49)$$

The baseline value (1.2) and amplitude ranges ( $A_j \in [0.5, 1.25]$ ) are increased compared to human-to-human transmission to reflect the stronger seasonal dependence of vector-borne diseases.

### Multi-Wave Dynamics

Similar to the human-to-human simulator, vector-borne outbreaks can exhibit multiple waves through time-varying transmission scaling:

$$\beta(t) = \beta_i \quad \text{for } t \in [t_{i-1}, t_i) \quad (50)$$

However, for vector-borne diseases, wave changes often reflect environmental conditions affecting vector populations (rainfall, temperature) or intervention campaigns rather than behavioral changes.

## Intervention Modeling

Vector control interventions are modeled through the reduction factor  $f_{intervention}(t)$  applied to both  $\lambda_h$  and  $\lambda_v$ . Common interventions include:

- **Vector control:** Reduces vector population or biting rates
- **Larvicide applications:** Affects vector reproduction
- **Personal protection:** Reduces effective contact rates
- **Environmental management:** Modifies vector habitat suitability

The intervention policy triggers based on human case thresholds but affects the vector reduction parameter:

$$f_{intervention}(t) = \begin{cases} f_{vector} & \text{if intervention active} \\ 1.0 & \text{otherwise} \end{cases} \quad (51)$$

where  $f_{vector} \in [0.2, 0.6]$  represents the effectiveness of vector control measures.

## Initialization Strategy

**Human Population** Initial conditions allow for pre-existing immunity in the human population:

$$\text{Immune fraction} \sim \text{Uniform}(0, 0.7) \quad (52)$$

$$\text{Initial infections} \sim \text{NegativeBinomial}(n = \max(1, N_h \times 5 \times 10^{-6}), p = 0.5) \quad (53)$$

**Vector Population** Vector populations start with a small fraction exposed/infected:

$$N_v = N_h \times \text{Uniform}(2.0, 10.0) \quad (54)$$

$$\text{Initial vector exposures} \sim \text{NegativeBinomial}(n = \max(1, N_v \times 10^{-4}), p = 0.3) \quad (55)$$

The higher initial prevalence in vectors reflects their role as reservoirs and their shorter generation times.

## Parameter Ranges

Table 2 summarizes all parameters specific to the vector-borne transmission simulator.

Table 2: Vector-Borne Transmission Simulator Parameters

Parameter	Symbol	Range/Distribution	Units
<b>Human Population (Shared with H2H)</b>			
Population size	$N_h$	Log-uniform[50,000, 40,000,000]	individuals
Base transmission scaling	$\beta$	Uniform[0.5, 0.7]	-
Recovery rate	$\gamma$	Uniform[0.1, 0.33]	$\text{day}^{-1}$
Latent progression rate	$\sigma_h$	Uniform[0.2, 0.4] [19]	$\text{day}^{-1}$
Waning immunity rate	$\omega$	Uniform[0.003, 0.02] [20]	$\text{day}^{-1}$
Asymptomatic probability	$p_a$	Beta(3, 7)	proportion
Asymp. transmissibility	$\alpha$	Beta(2, 5)	proportion
<b>Vector Population Dynamics</b>			

Continued on next page

**Table 2 – continued from previous page**

Parameter	Symbol	Range/Distribution	Units
Vector population size	$N_v$	$N_h \times \text{Uniform}[2.0, 10.0]$	individuals
Vector mortality rate	$\mu_v$	$\text{Uniform}[0.03, 0.10]$	$\text{day}^{-1}$
Vector latent progression	$\sigma_v$	$\text{Uniform}[0.15, 0.30]$	$\text{day}^{-1}$
Vector lifespan	$1/\mu_v$	$\text{Uniform}[10, 33]$	days
Extrinsic incubation	$1/\sigma_v$	$\text{Uniform}[3.3, 6.7]$	days
<b>Transmission Parameters</b>			
Biting rate	$a$	$\text{Uniform}[0.40, 0.80]$	bites/vector/day
Vector→human transmission	$b_h$	$\text{Uniform}[0.35, 0.75]$	probability
Human→vector transmission	$b_v$	$\text{Uniform}[0.35, 0.75]$	probability
<b>Model Structure Options</b>			
Has latent period	-	$\text{Bernoulli}(0.7)$	boolean
Has asymptomatic compartment	-	$\text{Bernoulli}(0.5)$	boolean
Has waning immunity	-	$\text{Bernoulli}(1.0)$	boolean
<b>Enhanced Seasonality</b>			
Use seasonality	-	$\text{Bernoulli}(0.8)$	boolean
Base seasonal value	-	1.2	-
Harmonic amplitude range	$A_j$	$\text{Base} \times \text{Uniform}[0.3, 1.0]$	proportion
Base amplitude	-	$\text{Uniform}[0.5, 1.25]$	proportion
Number of harmonics	$n_h$	$\text{Uniform}[1, 4]$	count
<b>Multi-Wave Dynamics</b>			
Multiple waves enabled	-	Configurable (default: True)	boolean
Number of wave changes	-	$\text{Uniform}[0, 4]$	count
Wave change timing	-	$\text{Uniform}[50, 1800]$	days
<b>Vector Control Interventions</b>			
Enable intervention	-	$\text{Bernoulli}(0.25)$	boolean
On threshold	-	$N_h \times \text{Uniform}[1e-5, 1e-3]$	cases/day
Off threshold	-	$\text{On threshold} \times \text{Uniform}[0, 1]$	cases/day
Vector reduction	$f_{vector}$	$\text{Uniform}[0.2, 0.6]$	proportion
Trigger delay	-	$\text{Uniform}[0, 21]$	days
Minimum duration	-	$\text{Uniform}[14, 35]$	days
Maximum duration	-	Choice[None, $\text{Uniform}[60, 120]$ ]	days
Consecutive off days	-	$\text{Uniform}[1, 50]$	days
<b>Initialization Parameters</b>			
Human immune fraction	-	$\text{Uniform}[0.0, 0.7]$	proportion
Initial human infections	-	$\text{NegBin}(n = \max(1, N_h \times 5e^{-6}), p = 0.5)$	count
Vector:human ratio	-	$\text{Uniform}[2.0, 10.0]$	ratio
Initial vector exposures	-	$\text{NegBin}(n = \max(1, N_v \times 1e^{-4}), p = 0.3)$	count
<b>Observation &amp; Outcomes (Shared)</b>			
Hospitalization probability	$p_h$	$\text{Uniform}[0.05, 0.20]$	proportion

Continued on next page

**Table 2 – continued from previous page**

Parameter	Symbol	Range/Distribution	Units
Death probability (of hosp.)	$p_d$	Uniform[0.10, 0.40]	proportion
Hosp. delay shape	$k_h$	Uniform[2.0, 4.0]	-
Hosp. delay scale	$\theta_h$	Uniform[1.0, 3.0]	days
Death delay shape	$k_d$	Uniform[1.5, 2.5]	-
Death delay scale	$\theta_d$	Uniform[2.0, 5.0]	days
<b>Noise &amp; Reporting (Identical to H2H)</b>			
Multiplicative noise std	$\sigma_{mult}$	0.1	log-scale
Reporting effects	-	Same as Table 1	various
Day-of-week effects	-	Same as Table 1	various
Lab noise parameters	-	Same as Table 1	various
Delay distributions	-	Same as Table 1	various

### Key Differences from Human-to-Human Transmission

The vector-borne simulator incorporates several critical differences that distinguish it from direct human-to-human transmission:

**Dual Population Dynamics** Unlike human-to-human models, vector-borne diseases require explicit modeling of vector population dynamics, including birth, death, and infection processes within the arthropod population.

**Transmission Pathway** Transmission requires a two-step process (human  $\rightarrow$  vector  $\rightarrow$  human) rather than direct contact, fundamentally altering the epidemic dynamics and introducing additional delay and complexity.

**Environmental Sensitivity** Vector-borne diseases exhibit stronger seasonal patterns due to vector ecology dependence on temperature, rainfall, and other environmental factors, reflected in enhanced seasonal forcing parameters.

**Vector-Specific Interventions** Control strategies focus on vector population reduction rather than behavioral modifications, affecting both  $\lambda_h$  and  $\lambda_v$  through environmental rather than social mechanisms.

**Basic Reproduction Number**  $R_0$  calculations must account for the round-trip transmission cycle and vector population dynamics, resulting in a more complex formulation that depends on vector:human ratios and vector survival probabilities.

This comprehensive parameter space enables realistic simulation of diverse vector-borne disease scenarios, capturing the full spectrum of arthropod-transmitted pathogen dynamics across different ecological contexts, intervention strategies, and surveillance systems.

### Environmental Transmission Simulator

The environmental transmission simulator implements a hybrid compartmental model that captures diseases transmitted through both direct human-to-human contact and indirect environmental pathways via contaminated water sources. This simulator models pathogens such as cholera, typhoid, hepatitis A, and norovirus, which exhibit complex transmission dynamics involving multiple routes of exposure and environmental persistence.

## Model Structure

**Dual-Route Transmission Framework** The waterborne model extends the basic SEAIR structure to include an additional environmental compartment representing pathogen concentration in water. The model simultaneously tracks both direct contact transmission (similar to respiratory diseases) and indirect transmission through contaminated water or environmental sources.

**Human Population Dynamics** The human compartments follow the same structure as the human-to-human model:

$$\frac{dS}{dt} = -\lambda_h S + \omega R + bN - dS \quad (56)$$

$$\frac{dE}{dt} = \lambda_h S - \sigma E - dE \quad (57)$$

$$\frac{dA}{dt} = p_a \sigma E - \gamma_a A - dA \quad (58)$$

$$\frac{dI}{dt} = (1 - p_a) \sigma E - \gamma I - dI \quad (59)$$

$$\frac{dR}{dt} = \gamma_a A + \gamma I - \omega R - dR \quad (60)$$

**Environmental Pathogen Dynamics** The environmental water compartment evolves according to:

$$\frac{dW}{dt} = \eta_I I + \eta_A A - \mu_w W \quad (61)$$

where:

- $W$ : Pathogen concentration in water sources
- $\eta_I$ : Contamination rate from symptomatic individuals
- $\eta_A$ : Contamination rate from asymptomatic individuals
- $\mu_w$ : Pathogen decay/removal rate in water

**Composite Force of Infection** The total force of infection combines both transmission routes:

$$\lambda_h(t) = \lambda_{contact}(t) + \lambda_{water}(t) \quad (62)$$

where:

$$\lambda_{contact}(t) = \beta(t) \cdot s(t) \cdot \frac{I + \alpha A}{N} \cdot f_{contact}(t) \quad (63)$$

$$\lambda_{water}(t) = \delta(t) \cdot s(t) \cdot W \cdot f_{water}(t) \quad (64)$$

The parameters are:

- $\beta(t)$ : Time-varying contact transmission rate
- $\delta(t)$ : Time-varying waterborne transmission rate
- $s(t)$ : Seasonal forcing factor (affects both routes)
- $f_{contact}(t), f_{water}(t)$ : Intervention effectiveness factors
- $\alpha$ : Relative transmissibility of asymptomatic individuals

## Multi-Route Wave Dynamics

Waterborne diseases can exhibit complex temporal patterns due to independent variation in both transmission routes. The model implements time-varying transmission coefficients for both pathways:

$$\beta(t) = \beta_i \quad \text{for } t \in [t_{i-1}, t_i] \quad (65)$$

$$\delta(t) = \delta_i \quad \text{for } t \in [t_{i-1}, t_i] \quad (66)$$

Wave changes can reflect:

- **Contact route changes:** Behavioral modifications, crowding patterns, hygiene practices
- **Water route changes:** Infrastructure failures, seasonal water quality, sanitation disruptions
- **Coordinated changes:** Public health interventions affecting both routes simultaneously

## Environmental Contamination Process

**Contamination Sources** Both symptomatic and asymptomatic individuals contribute to environmental contamination:

$$\text{Daily contamination} = \eta_I \cdot I + \eta_A \cdot A \cdot \alpha_{env} \quad (67)$$

where  $\eta_I$  and  $\eta_A$  represent base contamination rates, and  $\alpha_{env}$  is the relative environmental shedding from asymptomatic individuals.

**Pathogen Persistence and Decay** Environmental pathogens undergo exponential decay:

$$\frac{dW}{dt} \Big|_{\text{decay}} = -\mu_w W \quad (68)$$

The decay rate  $\mu_w$  encompasses multiple removal mechanisms:

- Natural pathogen die-off
- Water treatment processes
- Dilution effects
- UV radiation and temperature effects

## Stochastic Implementation

The continuous-time model is implemented stochastically with daily time steps:

## Human Transmission Events

$$\text{Contact exposures} \sim \text{Binomial}(S(t), 1 - e^{-\lambda_{contact}(t)}) \quad (69)$$

$$\text{Water exposures} \sim \text{Binomial}(S(t), 1 - e^{-\lambda_{water}(t)}) \quad (70)$$

$$\text{Total new exposures} = \text{Contact exposures} + \text{Water exposures} \quad (71)$$

Note: In the stochastic implementation, total exposures are calculated as:

$$\text{Total exposures} \sim \text{Binomial}(S(t), 1 - e^{-(\lambda_{contact}(t) + \lambda_{water}(t))}) \quad (72)$$

## Environmental Process Updates

$$\text{New contamination} = \eta_I \cdot I(t) + \eta_A \cdot A(t) \cdot \alpha_{env} \quad (73)$$

$$\text{Pathogen decay} = \mu_w \cdot W(t) \quad (74)$$

$$W(t+1) = \max(0, W(t) + \text{New contamination} - \text{Pathogen decay}) \quad (75)$$

**Compartment Transitions** Human compartment transitions follow the same binomial processes as the human-to-human model:

$$E \rightarrow I/A \sim \text{Binomial}(E(t), 1 - e^{-\sigma}) \quad (76)$$

$$\text{Recovery from } I \sim \text{Binomial}(I(t), 1 - e^{-\gamma}) \quad (77)$$

$$\text{Recovery from } A \sim \text{Binomial}(A(t), 1 - e^{-\gamma_a}) \quad (78)$$

$$\text{Waning immunity} \sim \text{Binomial}(R(t), 1 - e^{-\omega}) \quad (79)$$

## Enhanced Seasonality

Waterborne diseases exhibit strong seasonal patterns due to environmental factors affecting both transmission routes and pathogen survival:

$$s(t) = 1.0 + \sum_{j=1}^{n_h} A_j \cos\left(\frac{2\pi(t - \phi_j + \delta_y)}{P_j}\right) + \epsilon_t \quad (80)$$

**Seasonal Factors** Seasonality in waterborne diseases reflects:

- **Rainfall patterns:** Affecting water contamination and treatment efficacy
- **Temperature effects:** Influencing pathogen survival in water
- **Flooding events:** Disrupting sanitation infrastructure
- **Social patterns:** Seasonal migration, gatherings, and water usage

**Enhanced Amplitude Range** Waterborne diseases show stronger seasonal variation with amplitude parameters:

$$A_j \in [0.6, 1.5] \text{ (compared to } [0.1, 0.5] \text{ for human-to-human)} \quad (81)$$

## Dual-Route Intervention Modeling

Interventions can target either or both transmission routes with different effectiveness:

$$\lambda_{contact,eff}(t) = \lambda_{contact}(t) \cdot f_{contact}(t) \quad (82)$$

$$\lambda_{water,eff}(t) = \lambda_{water}(t) \cdot f_{water}(t) \quad (83)$$

**Contact Route Interventions** Similar to human-to-human diseases:

- Social distancing measures
- Hygiene promotion
- Isolation of cases

**Water Route Interventions** Specific to environmental transmission:

- Water treatment and chlorination
- Sanitation infrastructure improvements
- Safe water distribution
- Waste management systems

**Intervention Policy** The universal intervention policy can independently affect both routes:

$$f_{contact}(t) \in [0.2, 0.6] \text{ when intervention active} \quad (84)$$

$$f_{water}(t) \in [0.3, 0.7] \text{ when intervention active} \quad (85)$$

### Super-Spreading Events

Super-spreading affects only the contact transmission route, as waterborne transmission is mediated by environmental persistence rather than individual variation:

$$\lambda_{contact,ss}(t) = \lambda_{contact}(t) \cdot m_{ss}(t) \quad (86)$$

where  $m_{ss}(t)$  follows the same gamma-distributed multiplier as in human-to-human transmission.

### Initialization Strategy

**Human Population** Initial conditions allow for higher pre-existing immunity due to endemic circulation:

$$\text{Immune fraction} \sim \text{Beta}(10, 3.5) \text{ (higher mean than H2H)} \quad (87)$$

$$\text{Initial infections} \sim \text{NegativeBinomial}(n = N_h \times 10^{-6}, p = 0.5) \quad (88)$$

**Environmental Pathogen Load** The water compartment initializes at zero, building up through contamination from initial infections:

$$W(0) = 0 \quad (89)$$

### Parameter Ranges

Table 3 summarizes all parameters specific to the waterborne transmission simulator.

Table 3: Waterborne Transmission Simulator Parameters

Parameter	Symbol	Range/Distribution	Units
<b>Human Population (Shared)</b>			
Population size	$N$	Log-uniform[50,000, 40,000,000]	individuals
Recovery rate	$\gamma$	Uniform[0.1, 0.33]	day <sup>-1</sup>
Latent progression rate	$\sigma$	Uniform[0.2, 0.4]	day <sup>-1</sup>
Waning immunity rate	$\omega$	Uniform[0.001, 0.01]	day <sup>-1</sup>
Asymptomatic probability	$p_a$	Beta(3, 7)	proportion
Asymp. transmissibility	$\alpha$	Beta(2, 5)	proportion
<b>Dual-Route Transmission</b>			

Continued on next page

**Table 3 – continued from previous page**

Parameter	Symbol	Range/Distribution	Units
Contact transmission rate	$\beta$	Uniform[0.0, 0.05]	day <sup>-1</sup>
Water transmission rate	$\delta$	Uniform[0.0005, 0.01]	day <sup>-1</sup>
Water contamination rate	$\eta$	Uniform[0.001, 0.01]	day <sup>-1</sup>
Pathogen decay rate	$\mu_w$	Uniform[0.05, 0.3]	day <sup>-1</sup>
Pathogen half-life	$\ln(2)/\mu_w$	Uniform[2.3, 13.9]	days
<b>Model Structure Options</b>			
Has latent period	-	Bernoulli(0.7)	boolean
Has asymptomatic compartment	-	Bernoulli(0.6)	boolean
Has waning immunity	-	Bernoulli(0.9)	boolean
<b>Multi-Wave Dynamics</b>			
Multiple waves enabled	-	Configurable (default: True)	boolean
Number of wave changes	-	Uniform[0, 7]	count
Wave change timing	-	Uniform[50, 1800]	days
Contact wave segments	-	Wave count + 1	count
Water wave segments	-	Wave count + 1	count
<b>Enhanced Seasonality</b>			
Use seasonality	-	Bernoulli(0.9)	boolean
Number of harmonics	$n_h$	Uniform[1, 4]	count
Base amplitude	-	Uniform[0.6, 1.5]	proportion
Harmonic amplitude	$A_j$	Base $\times$ Uniform[0.3, 1.0]	proportion
Phase offset	$\phi_j$	Uniform[0, 365] + Uniform[-60, 60]	days
Possible periods	$P_j$	Choice[365.0, 182.5, 91.25]	days
Daily noise std	$\sigma_\epsilon$	0.05	proportion
Annual peak jitter	$\delta_y$	Uniform[-30, 30]	days
<b>Dual-Route Interventions</b>			
Enable intervention	-	Bernoulli(0.25)	boolean
On threshold	-	$N \times$ Uniform[1e-5, 1e-3]	cases/day
Off threshold	-	On threshold $\times$ Uniform[0, 1]	cases/day
Contact reduction	$f_{contact}$	Uniform[0.2, 0.6]	proportion
Water reduction	$f_{water}$	Uniform[0.3, 0.7]	proportion
Trigger delay	-	Uniform[0, 21]	days
Minimum duration	-	Uniform[14, 35]	days
Maximum duration	-	Choice[None, Uniform[60, 120]]	days
Consecutive off days	-	Uniform[1, 50]	days
<b>Super-Spreading (Contact Only)</b>			
Super-spreader probability	$p_{ss}$	Uniform[0.0002, 0.02]	proportion
Multiplier shape	$k_{ss}$	4.0	-
Multiplier scale	$\theta_{ss}$	1.5	-
<b>Endemic Demographics</b>			
Enable endemic	-	Bernoulli(0.8)	boolean
Birth rate	$b$	Uniform[0.00002, 0.00012]	day <sup>-1</sup>
Death rate factor	-	Uniform[0.8, 1.3]	proportion
Importation rate	$\iota$	Exp(Uniform[ln(0.01), ln(0.5)])	day <sup>-1</sup>

Continued on next page

**Table 3 – continued from previous page**

Parameter	Symbol	Range/Distribution	Units
<b>Initialization Parameters</b>			
Novel outbreak probability	-	0.0 (always endemic)	proportion
Immune fraction (if endemic)	-	Beta(10, 3.5)	proportion
Initial infections	-	NegBin( $n = N \times 10^{-6}$ , $p = 0.5$ )	count
Initial water pathogen load	$W(0)$	0.0	concentration
<b>Observation &amp; Outcomes</b>			
Hospitalization probability	$p_h$	Uniform[0.02, 0.15]	proportion
Death probability (of hosp.)	$p_d$	Uniform[0.05, 0.3]	proportion
Hosp. delay shape	$k_h$	Uniform[2.0, 4.0]	-
Hosp. delay scale	$\theta_h$	Uniform[1.0, 3.0]	days
Death delay shape	$k_d$	Uniform[1.5, 2.5]	-
Death delay scale	$\theta_d$	Uniform[2.0, 5.0]	days
<b>Noise &amp; Reporting (Identical to H2H)</b>			
Multiplicative noise std	$\sigma_{mult}$	0.1	log-scale
Overdispersion parameter	$r$	100	-
Reporting effects	-	Same as Table 1	various
Day-of-week effects	-	Same as Table 1	various
Lab noise parameters	-	Same as Table 1	various
Delay distributions	-	Same as Table 1	various

### Key Differences from Other Transmission Modes

The waterborne simulator incorporates several distinguishing features:

**Dual Transmission Pathways** Unlike single-route models, waterborne diseases require simultaneous modeling of direct contact and environmental transmission, each with independent temporal dynamics and intervention susceptibilities.

**Environmental Persistence** The explicit water compartment captures pathogen persistence in the environment, creating temporal delays and amplification effects not present in direct transmission models.

**Route-Specific Interventions** Control strategies must address both transmission pathways, with water-focused interventions (treatment, sanitation) having different effectiveness profiles than contact-focused measures.

**Enhanced Seasonal Dependence** Environmental factors create stronger seasonal patterns than purely social transmission modes, reflected in increased amplitude ranges and environmental sensitivity.

**Endemic Circulation Patterns** Higher baseline immunity levels reflect the endemic nature of many waterborne diseases in affected populations, influencing outbreak dynamics and intervention effectiveness.

This comprehensive dual-route framework enables realistic simulation of waterborne disease dynamics across diverse environmental contexts, intervention strategies, and population immunity profiles, capturing the complex interplay between direct and indirect transmission pathways characteristic of environmentally-mediated pathogens.

## B Model Architecture

Mantis is implemented as a hybrid convolutional-transformer architecture specifically designed for epidemiological time series forecasting. The model consists of five main components: (1) multi-scale input embeddings, (2) hybrid CNN-transformer encoder blocks, (3) an epidemic pattern memory bank, (4) an autoregressive quantile decoder, and (5) comprehensive temporal feature engineering. This section provides detailed specifications for each component.

### B.1 Input Processing and Feature Engineering

#### B.1.1 Multi-Scale Convolutional Embedding

The input embedding layer processes time series data using parallel convolutions at multiple temporal scales to capture epidemiological patterns across different time horizons. For input tensor  $\mathbf{X} \in \mathbb{R}^{B \times L \times 2}$  where  $B$  is batch size,  $L$  is sequence length, and the feature dimension includes both target values and covariates (e.g., deaths and hospitalizations), the multi-scale embedding applies four parallel 1D convolutions:

$$\mathbf{H}_{\text{short}} = \text{Conv1D}(\mathbf{X}; k = 3, d_{\text{out}} = d/4) \quad (90)$$

$$\mathbf{H}_{\text{med}} = \text{Conv1D}(\mathbf{X}; k = 7, d_{\text{out}} = d/4) \quad (91)$$

$$\mathbf{H}_{\text{long}} = \text{Conv1D}(\mathbf{X}; k = 15, d_{\text{out}} = d/4) \quad (92)$$

$$\mathbf{H}_{\text{vlong}} = \text{Conv1D}(\mathbf{X}; k = 31, d_{\text{out}} = d/4) \quad (93)$$

where  $k$  denotes kernel size,  $d$  is the target hidden dimension (default 512), and each convolution uses appropriate padding to maintain sequence length. Each scale captures different temporal patterns:

- Short-term ( $k=3$ ): Weekly variations and immediate trends
- Medium-term ( $k=7$ ): Monthly patterns and intervention responses
- Long-term ( $k=15$ ): Seasonal cycles and extended epidemic phases
- Very long-term ( $k=31$ ): Annual seasonality and yearly trends

Each convolutional output is independently normalized and activated:

$$\tilde{\mathbf{H}}_i = \text{Dropout}(\text{SiLU}(\text{LayerNorm}(\mathbf{H}_i))) \quad \text{for } i \in \{\text{short, med, long, vlong}\} \quad (94)$$

The multi-scale features are concatenated and projected to the target hidden dimension:

$$\mathbf{H}_{\text{conv}} = \text{LayerNorm}(\mathbf{W}_{\text{proj}} \cdot \text{Concat}([\tilde{\mathbf{H}}_{\text{short}}, \tilde{\mathbf{H}}_{\text{med}}, \tilde{\mathbf{H}}_{\text{long}}, \tilde{\mathbf{H}}_{\text{vlong}}])) \quad (95)$$

where  $\mathbf{W}_{\text{proj}} \in \mathbb{R}^{d \times d}$  is a learned projection matrix.

#### B.1.2 Static and Temporal Feature Embeddings

Mantis incorporates rich contextual information through multiple embedding layers:

**Disease Type Embedding** Disease categories are embedded using a learned lookup table:

$$\mathbf{e}_{\text{disease}} = \text{Embedding}(\text{disease\_type}; |V| = 3, d_{\text{disease}} = 64) \quad (96)$$

where the three disease types correspond to human-to-human, waterborne, and vector-borne transmission modes from the training simulations.

**Population Embedding** Population size is processed through a multi-layer perceptron after log-normalization:

$$\mathbf{e}_{\text{pop}} = \text{GELU}(\text{LayerNorm}(\mathbf{W}_{\text{pop}} \cdot \log(1 + \text{population}))) \quad (97)$$

where  $\mathbf{W}_{\text{pop}} \in \mathbb{R}^{64 \times 1}$  projects the scalar population to a 64-dimensional embedding.

**Enhanced Temporal Embeddings** Temporal patterns are captured through multiple cyclic embeddings derived from absolute day indices. For day index  $d_t$  at timestep  $t$ :

$$\mathbf{e}_{\text{dow}} = \text{LayerNorm}(\text{Embedding}(d_t \bmod 7; |V| = 7, d = 128)) \quad (98)$$

$$\mathbf{e}_{\text{month}} = \text{LayerNorm}(\text{Embedding}(\lfloor d_t/30 \rfloor \bmod 12; |V| = 12, d = 128)) \quad (99)$$

$$\mathbf{e}_{\text{doy}} = \text{LayerNorm}(\text{Embedding}(d_t \bmod 366; |V| = 366, d = 128)) \quad (100)$$

These embeddings capture day-of-week effects (reporting cycles), monthly seasonality, and annual patterns respectively.

### B.1.3 Feature Integration

All embedding components are concatenated and projected to the model’s hidden dimension. Static embeddings are expanded across the temporal dimension:

$$\mathbf{H}_{\text{input}} = \text{LayerNorm}(\mathbf{W}_{\text{feat}} \cdot \text{Concat}([\mathbf{H}_{\text{conv}}, \mathbf{E}_{\text{disease}}, \mathbf{E}_{\text{pop}}, \mathbf{e}_{\text{dow}}, \mathbf{e}_{\text{month}}, \mathbf{e}_{\text{doy}}])) \quad (101)$$

where  $\mathbf{E}_{\text{disease}}, \mathbf{E}_{\text{pop}} \in \mathbb{R}^{B \times L \times d_{\text{embed}}}$  are the temporally expanded static embeddings, and  $\mathbf{W}_{\text{feat}} \in \mathbb{R}^{d \times (d+64+64+128+128+128)}$  projects the concatenated features to hidden dimension  $d$ .

## B.2 Hybrid CNN-Transformer Encoder

The encoder consists of  $N$  stacked hybrid blocks (default  $N = 16$ ), each combining local convolutional processing with global attention mechanisms.

### B.2.1 Temporal Pattern Attention

Each encoder block uses a custom attention mechanism (‘TemporalPatternAttention’) that incorporates relative positional encoding specifically designed for temporal sequences:

$$\mathbf{Q}, \mathbf{K}, \mathbf{V} = \mathbf{HW}_Q, \mathbf{HW}_K, \mathbf{HW}_V \quad (102)$$

$$\mathbf{A}_{i,j} = \frac{\mathbf{Q}_i \mathbf{K}_j^T}{\sqrt{d_k}} + \mathbf{R}_{i-j+L-1} \quad (103)$$

$$\text{Attention}(\mathbf{H}) = \text{softmax}(\mathbf{A}) \mathbf{V} \quad (104)$$

where  $\mathbf{R} \in \mathbb{R}^{2L-1 \times h}$  is a learned relative positional bias matrix with  $h$  attention heads, and  $\mathbf{R}_{i-j+L-1}$  provides position-dependent bias for the attention score between positions  $i$  and  $j$ .

The relative positional encoding allows the model to learn temporal relationships that are translation-invariant, which is crucial for epidemiological patterns that may occur at different absolute times but with similar relative timing.

### B.2.2 CNN-Transformer Hybrid Block

Each encoder block (‘CNNTransformerBlock’) follows a three-stage design with post-normalization:

#### Stage 1: Local Pattern Extraction

$$\mathbf{H}^{(1)} = \text{LayerNorm}(\mathbf{H}^{(0)} + \text{Dropout}(\text{LocalConv}(\mathbf{H}^{(0)}))) \quad (105)$$

where LocalConv applies depthwise separable convolution:

$$\text{LocalConv}(\mathbf{H}) = \text{Conv1D}(\text{DepthwiseConv1D}(\mathbf{H}; k = 5); k = 1) \quad (106)$$

The depthwise convolution (kernel size 5) captures local temporal dependencies within each feature channel, followed by a pointwise convolution that mixes information across channels.

### Stage 2: Global Context Attention

$$\mathbf{H}^{(2)} = \text{LayerNorm}(\mathbf{H}^{(1)} + \text{Dropout}(\text{TemporalPatternAttention}(\mathbf{H}^{(1)}, \mathbf{M}))) \quad (107)$$

where  $\mathbf{M} \in \{0, 1\}^{B \times L}$  is the padding mask indicating valid sequence positions.

### Stage 3: Position-wise Feed-Forward

$$\mathbf{H}^{(3)} = \text{LayerNorm}(\mathbf{H}^{(2)} + \text{Dropout}(\text{FFN}(\mathbf{H}^{(2)}))) \quad (108)$$

where the feed-forward network is:

$$\text{FFN}(\mathbf{H}) = \mathbf{W}_2 \text{GELU}(\mathbf{W}_1 \mathbf{H} + \mathbf{b}_1) + \mathbf{b}_2 \quad (109)$$

with  $\mathbf{W}_1 \in \mathbb{R}^{d \times d_{\text{ffn}}}$ ,  $\mathbf{W}_2 \in \mathbb{R}^{d_{\text{ffn}} \times d}$ , and  $d_{\text{ffn}} = 2048$  by default.

## B.3 Epidemic Pattern Memory Bank

The pattern memory module ('EpidemicPatternMemory') implements a learnable memory bank that stores prototypical epidemic patterns discovered during training.

### B.3.1 Pattern Bank Initialization

The pattern bank consists of  $K = 256$  learnable pattern vectors:

$$\mathbf{P} = [\mathbf{p}_1, \mathbf{p}_2, \dots, \mathbf{p}_K] \in \mathbb{R}^{K \times d} \quad (110)$$

Pattern vectors are initialized with small random values:  $\mathbf{p}_k \sim \mathcal{N}(0, 0.02^2 \mathbf{I})$ .

### B.3.2 Pattern Matching and Retrieval

For encoder output  $\mathbf{H}_{\text{enc}} \in \mathbb{R}^{B \times L \times d}$ , pattern matching computes attention weights over the pattern bank:

$$\mathbf{S} = \text{FFN}_{\text{match}}(\text{LayerNorm}(\mathbf{H}_{\text{enc}})) \in \mathbb{R}^{B \times L \times K} \quad (111)$$

$$\mathbf{A}_{\text{pattern}} = \text{softmax}(\mathbf{S} \odot \mathbf{M}_{\text{exp}}) \quad (112)$$

$$\mathbf{H}_{\text{retrieved}} = \mathbf{A}_{\text{pattern}} \mathbf{P} \in \mathbb{R}^{B \times L \times d} \quad (113)$$

where  $\mathbf{M}_{\text{exp}} \in \mathbb{R}^{B \times L \times 1}$  is the expanded padding mask,  $\odot$  denotes element-wise multiplication, and  $\text{FFN}_{\text{match}}$  is a two-layer network:

$$\text{FFN}_{\text{match}}(\mathbf{x}) = \mathbf{W}_3 \text{GELU}(\mathbf{W}_4 \mathbf{x}) \quad (114)$$

with  $\mathbf{W}_4 \in \mathbb{R}^{d \times d}$  and  $\mathbf{W}_3 \in \mathbb{R}^{d \times K}$ .

### B.3.3 Pattern Integration

Retrieved patterns are projected and integrated with the encoder output using residual connections:

$$\mathbf{H}_{\text{memory}} = \text{LayerNorm}(\mathbf{H}_{\text{enc}} + \text{Dropout}(\mathbf{W}_{\text{proj}} \mathbf{H}_{\text{retrieved}})) \quad (115)$$

where  $\mathbf{W}_{\text{proj}} \in \mathbb{R}^{d \times d}$  is a learned projection matrix.

## B.4 Autoregressive Quantile Decoder

The decoder generates probabilistic forecasts using an autoregressive approach with a two-layer GRU and cross-attention to encoder memory.

### B.4.1 Decoder Initialization

The decoder state is initialized using masked pooling of the encoder output:

$$\mathbf{h}_0 = \mathbf{W}_{\text{init}} \cdot \text{MaskedPool}(\mathbf{H}_{\text{memory}}, \mathbf{M}) \quad (116)$$

$$\text{MaskedPool}(\mathbf{H}, \mathbf{M}) = \frac{\sum_{t=1}^L \mathbf{M}_{:,t} \odot \mathbf{H}_{:,t,:}}{\sum_{t=1}^L \mathbf{M}_{:,t} + \epsilon} \quad (117)$$

where  $\mathbf{W}_{\text{init}} \in \mathbb{R}^{d \times d}$  and  $\epsilon = 10^{-10}$  prevents division by zero. The initial state is replicated for the two-layer GRU:  $\mathbf{h}_0^{(1)} = \mathbf{h}_0^{(2)} = \mathbf{h}_0$ .

### B.4.2 Autoregressive Generation

For each forecast step  $\tau \in \{1, 2, \dots, H\}$  where  $H$  is the forecast horizon:

**Step 1: Input Processing** The previous prediction  $y_{\tau-1}$  is embedded:

$$\mathbf{e}_\tau = \text{GELU}(\text{LayerNorm}(\mathbf{W}_{\text{input}} y_{\tau-1})) \in \mathbb{R}^{B \times d/4} \quad (118)$$

**Step 2: Cross-Attention** The top GRU layer output attends to encoder memory:

$$\mathbf{q}_\tau = (\mathbf{h}_{\tau-1}^{(2)})^T \in \mathbb{R}^{B \times 1 \times d} \quad (119)$$

$$\mathbf{c}_\tau = \text{MultiHeadAttention}(\mathbf{q}_\tau, \mathbf{H}_{\text{memory}}, \mathbf{H}_{\text{memory}}, \neg \mathbf{M}) \quad (120)$$

where  $\neg \mathbf{M}$  serves as the key padding mask (True for padded positions).

**Step 3: GRU Update** The concatenated input is processed through the two-layer GRU:

$$\mathbf{x}_\tau = \text{Concat}([\mathbf{c}_\tau, \mathbf{e}_\tau]) \in \mathbb{R}^{B \times 1 \times (d+d/4)} \quad (121)$$

$$\mathbf{h}_\tau^{(1)}, \mathbf{h}_\tau^{(2)} = \text{GRU}(\mathbf{x}_\tau, [\mathbf{h}_{\tau-1}^{(1)}, \mathbf{h}_{\tau-1}^{(2)}]) \quad (122)$$

**Step 4: Quantile Prediction** Nine quantiles are predicted using separate projection heads:

$$\hat{q}_\tau^{(i)} = \mathbf{W}_{\text{out}}^{(i)} \text{GELU}(\text{LayerNorm}(\mathbf{W}_{\text{hidden}}^{(i)} \mathbf{h}_\tau^{(2)})) \quad (123)$$

$$\text{for } i \in \{1, 2, \dots, 9\} \quad (124)$$

where each quantile head has parameters  $\mathbf{W}_{\text{hidden}}^{(i)} \in \mathbb{R}^{(d/2) \times d}$  and  $\mathbf{W}_{\text{out}}^{(i)} \in \mathbb{R}^{1 \times (d/2)}$ . The nine quantiles correspond to percentiles: [5, 10, 25, 40, 50, 60, 75, 90, 95].

### B.4.3 Teacher Forcing

During training, teacher forcing is applied with linearly decaying probability:

$$p_{\text{tf}}(s) = p_{\text{initial}} \cdot \left(1 - \frac{s}{S_{\text{total}}}\right) + p_{\text{final}} \cdot \frac{s}{S_{\text{total}}} \quad (125)$$

where  $s$  is the current training step,  $S_{\text{total}}$  is the total number of training steps,  $p_{\text{initial}} = 0.2$ , and  $p_{\text{final}} = 0.0$ .

At each step, with probability  $p_{\text{tf}}(s)$ , the true target value is used as input instead of the model's prediction:

$$y_\tau = \begin{cases} \text{target}_\tau & \text{if } U(0, 1) < p_{\text{tf}}(s) \text{ and training} \\ \hat{q}_\tau^{(5)} & \text{otherwise (median prediction)} \end{cases} \quad (126)$$

## B.5 Training Configuration

### B.5.1 Weight Initialization

Model parameters are initialized using a careful scheme to ensure stable training:

$$\mathbf{W}_{\text{linear}} \sim \text{Xavier uniform with gain 0.01} \quad (127)$$

$$\mathbf{b} = \mathbf{0} \quad (128)$$

$$\mathbf{E}_{\text{embedding}} \sim \mathcal{N}(0, 0.01^2) \quad (129)$$

$$\mathbf{P}_{\text{pattern}} \sim \mathcal{N}(0, 0.02^2) \quad (130)$$

### B.5.2 Loss Function

The model is trained using quantile loss (pinball loss) averaged across all quantiles:

$$\mathcal{L}_{\text{quantile}} = \frac{1}{BH|Q|} \sum_{b=1}^B \sum_{\tau=1}^H \sum_{q \in Q} \rho_q(y_{b,\tau} - \hat{q}_{b,\tau}^{(q)}) \quad (131)$$

$$\rho_q(e) = \max(qe, (q-1)e) \quad (132)$$

where  $Q = \{0.05, 0.1, 0.25, 0.4, 0.5, 0.6, 0.75, 0.9, 0.95\}$  is the set of quantile levels, and  $e$  is the prediction error.

### B.5.3 Optimization

The model is trained using AdamW optimizer with OneCycle learning rate scheduling:

$$\text{AdamW} : \beta_1 = 0.9, \beta_2 = 0.999, \text{weight decay} = 0.01 \quad (133)$$

$$\text{OneCycle} : \text{max\_lr} = 10^{-4}, \text{pct\_start} = 0.05, \quad (134)$$

$$\text{div\_factor} = 10.0, \text{final\_div\_factor} = 100.0 \quad (135)$$

Gradient clipping is applied with maximum norm 1.0, and training uses gradient accumulation every 64 steps to simulate larger effective batch sizes.

## B.6 Model Scale and Efficiency

The full model configuration uses:

- Hidden dimension:  $d = 1024$
- Feed-forward dimension:  $d_{\text{ffn}} = 2048$
- Number of encoder layers:  $N = 16$
- Number of attention heads:  $h = 16$
- Pattern memory size:  $K = 256$
- Total parameters: approximately 150M

Training requires approximately 2 days on a single NVIDIA L4 GPU for one complete pass through the synthetic dataset (we only train with one epoch, since we can generate as much data as we need), while inference can be performed in real-time on standard hardware.

## C Evaluation Data

After training, Mantis is evaluated on real-world forecasting tasks spanning multiple diseases, regions, and targets. For each task, the model is run out-of-the-box: no retraining, fine-tuning, or exposure to real data is performed. Forecast accuracy is assessed using both pointwise metrics such as mean absolute error (MAE) and probabilistic calibration metrics based on quantile coverage (Appendix D.1). Mantis’s performance is compared to established forecasting benchmarks, including the CDC Forecast Hub ensemble and individual submissions [4], as well as published models such as Chronos [15].

### C.1 Primary Evaluation Tasks

#### C.1.1 Seasonal Influenza Hospitalizations in Michigan

We evaluated Mantis on weekly influenza hospitalization forecasts across Michigan’s eight public health preparedness regions during the 2023–2024 influenza season (August 2023 to August 2024). These regions are defined by the Michigan Department of Health and Human Services and represent heterogeneous groups of counties used for emergency response coordination. The regions vary substantially in population size (ranging from approximately 200,000 to 2.5 million residents), demographic composition, healthcare infrastructure, and urbanization levels, providing a diverse testbed for sub-state forecasting performance.

##### Data Characteristics

- **Temporal Coverage:** Weekly data from August 2023 through August 2024 (52 weeks)
- **Geographic Resolution:** 8 public health preparedness regions within Michigan (see figure 5)
- **Outcome Variable:** Weekly influenza hospitalizations
- **Population Range:** 200,000 to 2.5 million per region
- **Total Forecasts:** Approximately 2,080 individual forecasts across all regions and horizons

**Baseline Models** Disease-specific baselines included purpose-built models trained using all available historical data from November 2020 through the beginning of the evaluation period:

- **Michigan-optimized influenza model:** A hybrid CNN-transformer architecture developed through extensive iterative refinement by our group and University of Michigan collaborators, specifically tuned for regional influenza hospitalization forecasting
- **SARIMA models:** Seasonally adjusted autoregressive integrated moving average models with parameters selected via AIC optimization
- **LSTM networks:** Long short-term memory networks with architecture optimization
- **Chronos:** General-purpose time-series foundation model for comparison

#### C.1.2 COVID-19 Mortality Across U.S. States

To assess generalization to novel outbreak scenarios, we evaluated Mantis on weekly COVID-19 death forecasts across all 50 U.S. states, the District of Columbia, and Puerto Rico during the first two years of the pandemic (April 2020 through November 2021). This evaluation period matches the timeframe used in [4], enabling direct comparison with published CDC COVID-19 Forecast Hub results.

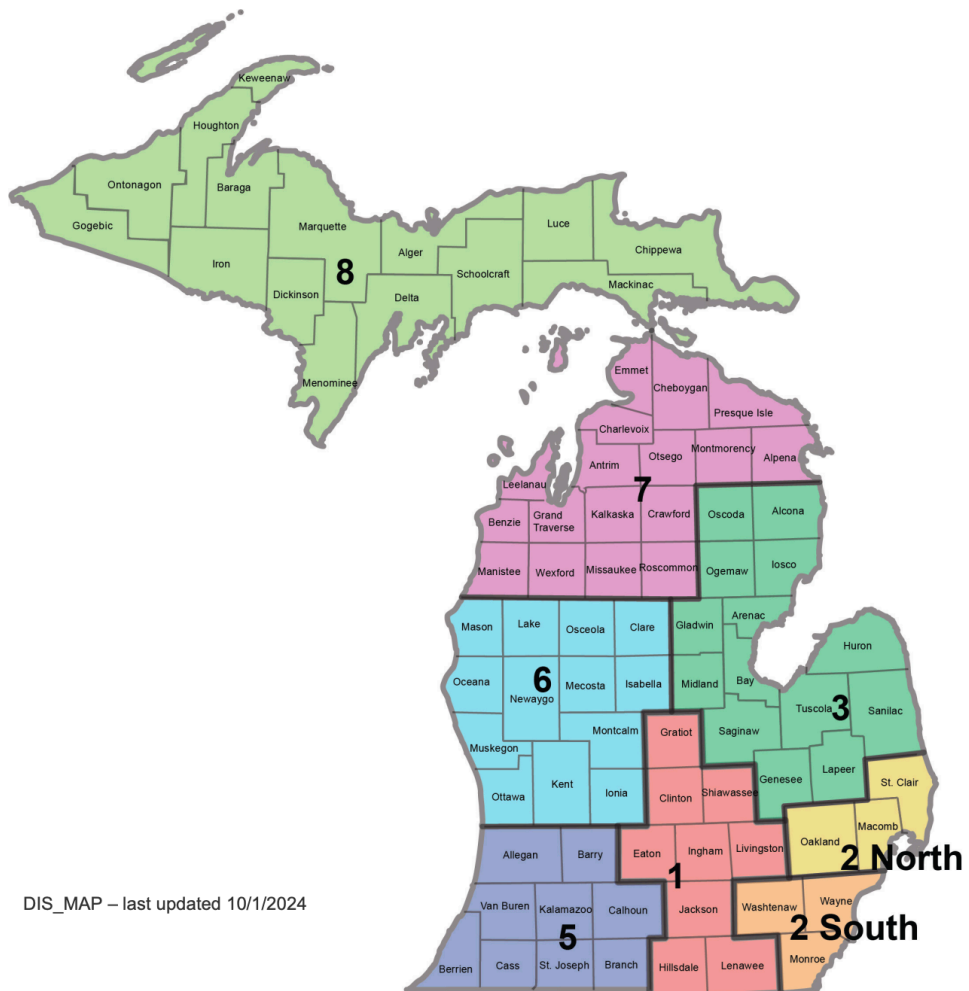


Figure 5: Public health preparedness regions within Michigan [21].

## Data Characteristics

- **Temporal Coverage:** Weekly data from April 2020 through November 2021 (87 weeks)
- **Geographic Resolution:** 52 jurisdictions (50 states + DC + Puerto Rico)
- **Outcome Variable:** Weekly COVID-19 deaths
- **Population Range:** 580,000 (Wyoming) to 39.5 million (California)
- **Total Forecasts:** Approximately 22,776 individual forecasts across all jurisdictions and horizons
- **Data Source:** CDC COVID-19 surveillance data [10]

**Baseline Comparisons** We benchmarked against models from the U.S. CDC COVID-19 Forecast Hub, which represented expert-curated approaches from modeling teams throughout the pandemic:

- **CDC Forecast Hub ensemble:** Weighted combination of top-performing individual models
- **Individual Hub models:** 28 distinct modeling approaches including statistical, mechanistic, and machine learning methods
- **Covariate utilization:** Most models incorporated extensive covariate information including case counts, mobility data, and syndromic surveillance signals
- **Continuous retraining:** Baselines were retrained as new data became available, reflecting operational practice

## C.2 Distribution Shift Evaluation Tasks

To further assess generalization capabilities under varying degrees of distribution shift, we conducted four additional evaluations on diseases and contexts that challenge different aspects of model robustness.

### C.2.1 Dengue Fever in Brazil (Vector-Borne Transmission)

We evaluated Mantis on dengue fever case forecasting across Brazilian states from 1993 to 2005, representing real-world vector-borne transmission dynamics within the model's training distribution.

#### Data Characteristics

- **Temporal Coverage:** Monthly data from 1993 through 2005 (156 months)
- **Geographic Resolution:** Alagoas, Brazil
- **Outcome Variable:** Monthly dengue fever cases
- **Population Range:** Roughly 3 million
- **Total Forecasts:** Approximately 4,096 individual forecasts
- **Data Source:** Project Tycho [11]
- **Transmission Mode:** Vector-borne (included in training simulations)

### C.2.2 Scarlet Fever in the United States (Historical Context)

Scarlet fever forecasting across U.S. states from 1910 to 1950 represents historical surveillance contexts with limited infrastructure and irregular reporting patterns.

### Data Characteristics

- **Temporal Coverage:** Weekly data from 1910 through 1950 (40 years)
- **Geographic Resolution:** 48 contiguous U.S. states (Alaska and Hawaii not yet states)
- **Outcome Variable:** Weekly scarlet fever cases
- **Population Range:** 200,000 to 10 million per state (1910-1950 demographics)
- **Total Forecasts:** Approximately 70,560 individual forecasts
- **Data Source:** Project Tycho [14]
- **Distribution Shift:** Early 20th-century surveillance systems with limited medical infrastructure

#### C.2.3 Hepatitis B in the United States (Blood-Borne Transmission)

Hepatitis B forecasting across U.S. states from 1978 to 1988 represents chronic blood-borne infections with long latency periods—a transmission mode explicitly excluded from Mantis’s training data.

### Data Characteristics

- **Temporal Coverage:** Weekly data from 1978 through 1988 (11 years)
- **Geographic Resolution:** 50 U.S. states
- **Outcome Variable:** Weekly hepatitis B cases
- **Population Range:** 400,000 to 25 million per state (1980s demographics)
- **Total Forecasts:** Approximately 57,344 individual forecasts
- **Data Source:** Project Tycho [12]
- **Distribution Shift:** Chronic blood-borne transmission not included in training simulations

#### C.2.4 Smallpox in the United States (Eradicated Disease)

Smallpox forecasting across U.S. states from 1925 to 1933 represents an eradicated disease with no modern analog in the training dataset.

### Data Characteristics

- **Temporal Coverage:** Weekly data from 1925 through 1933 (9 years)
- **Geographic Resolution:** 48 contiguous U.S. states
- **Outcome Variable:** Weekly smallpox cases
- **Population Range:** 500,000 to 12 million per state (1920s-1930s demographics)
- **Total Forecasts:** Approximately 21,888 individual forecasts
- **Data Source:** Project Tycho [13]
- **Distribution Shift:** Eradicated disease with no training analog; pre-vaccine era dynamics

#### C.2.5 Influenza-Like Illness (ILI) in the United States (Syndromic Data)

ILI forecasting across U.S. states from 2013 to 2025 represents a challenge to Mantis due to the lack of syndromic indicators in its training set.

## Data Characteristics

- **Temporal Coverage:** Weekly data from 2013 through 2025 (13 years)
- **Geographic Resolution:** 50 U.S. states, Washington D.C., and Puerto Rico.
- **Outcome Variable:** Weekly percentage of outpatient visits due to ILI.
- **Population Range:** 500,000 to 40 million per state
- **Total Forecasts:** Approximately 35,000 individual forecasts
- **Data Source:** CMU DELPHI [22]
- **Distribution Shift:** Syndromic indicator is a data type not seen during training

## C.3 Baseline Model Implementations

For the distribution shift evaluation tasks, we implemented strong statistical baselines to establish performance benchmarks:

### C.3.1 Naïve Persistence Model

The persistence model assumes that future values will equal the most recent observed value:

$$\hat{y}_{t+h} = y_t \quad \text{for all forecast horizons } h \quad (136)$$

### C.3.2 Exponential Smoothing (ETS)

We implemented exponential smoothing models with optimal configuration selection via Akaike Information Criterion (AIC). For each disease and forecast window, we evaluated a comprehensive range of ETS variants:

- **Error types:** Additive and multiplicative
- **Trend types:** None, additive, additive damped, multiplicative, multiplicative damped
- **Seasonal types:** None, additive, multiplicative
- **Training procedure:** Rolling forecasts with 104 weeks (or maximum available) of historical context
- **Model selection:** Best configuration selected per disease based on AIC across training period

## C.4 Data Preprocessing and Quality Control

### C.4.1 Standardization

All time series were preprocessed using consistent procedures:

- **Missing value handling:** Linear interpolation for isolated missing points; exclusion of series with  $\geq 10\%$  missing data (this leads to most states being excluded for the historical diseases)
- **Minimum length requirements:** Series with  $\leq 52$  observations excluded from evaluation

### C.4.2 Forecast Windows

Evaluation employed rolling forecast windows with consistent protocols:

- **Context length:** Up to 112 weeks of historical data for model input
- **Forecast horizons:** 4 and 8 weeks ahead for primary tasks; 8 weeks for distribution shift tasks
- **Rolling evaluation:** New forecasts generated weekly/monthly as new data became available
- **Evaluation metrics:** Mean Absolute Error (MAE), Mean Absolute Percentage Error (MAPE), 90% prediction interval coverage

## C.5 Evaluation Scope Summary

Table 4 summarizes the complete evaluation framework, highlighting the diversity of diseases, transmission modes, geographic scales, and temporal contexts covered in our assessment.

Table 4: Summary of Mantis Evaluation Framework

Disease	Location	Period	Frequency	Transmission	Distribution Shift
Influenza	Michigan regions	2023-2024	Weekly	Respiratory	None (in-distribution)
COVID-19	U.S. states/territories	2020-2021	Weekly	Respiratory	Novel pathogen
Dengue	Brazilian states	1993-2005	Monthly	Vector-borne	None (in-distribution)
Scarlet fever	U.S. states	1910-1950	Annual	Respiratory	Historical context
Hepatitis B	U.S. states	1978-1988	Annual	Blood-borne	Excluded transmission
Smallpox	U.S. states	1925-1933	Annual	Respiratory	Eradicated disease

This comprehensive evaluation framework enables robust assessment of Mantis’s forecasting capabilities across the full spectrum of infectious disease scenarios, from routine seasonal diseases to novel outbreaks and historically eradicated pathogens. The combination of primary tasks (representing operational forecasting scenarios) and distribution shift challenges (testing model robustness) provides a thorough evaluation of the simulation-grounded approach’s generalization capabilities.

## D Additional Results

### D.1 Mantis Delivers Well-Calibrated Uncertainty for Reliable Decision-Making

Accurate point forecasts alone are insufficient for public health planning—decision-makers require reliable uncertainty estimates to assess risk and allocate resources appropriately. A well-calibrated forecasting model should produce prediction intervals that contain the true values at their stated coverage rates: 50% intervals should capture observations half the time, and 90% intervals should capture observations nine times out of ten. Poor calibration undermines trust and can lead to systematic over- or under-preparation for outbreak scenarios.

We evaluated Mantis’s calibration across all diseases by comparing the predicted coverage rates of its uncertainty intervals to their empirical coverage in real-world data. For each disease and forecast horizon, we computed the proportion of observations that fell within the model’s 50% and 90% prediction intervals, then compared these empirical rates to the nominal 50% and 90% targets.

Table 5 shows that Mantis achieves excellent calibration across diverse diseases and transmission modes. Across all evaluation tasks, empirical coverage closely matches nominal coverage, with most diseases showing coverage within 2-3 percentage points of the target rates. This consistency holds across respiratory diseases (influenza, COVID-19), vector-borne diseases (dengue), and even historically eradicated pathogens (smallpox), demonstrating that simulation-based pretraining enables not only accurate point forecasts but also reliable uncertainty quantification. We visualize forecasts with both 50% and 90% CIs in figure 6.

Table 5: Prediction Interval Calibration Across Diseases

Disease	50% Coverage	90% Coverage
COVID-19 Mortality	51%	86%
COVID-19 Hospitalizations	53%	88%
Influenza Hospitalizations	51%	88%
Dengue Cases	47%	88%
Scarlet Fever	47%	88%
Hepatitis B	47%	85%
Smallpox	45%	82%

This calibration quality is essential for operational deployment. Public health officials must trust that when Mantis indicates a 90% probability that hospitalizations will fall within a specified range, that range

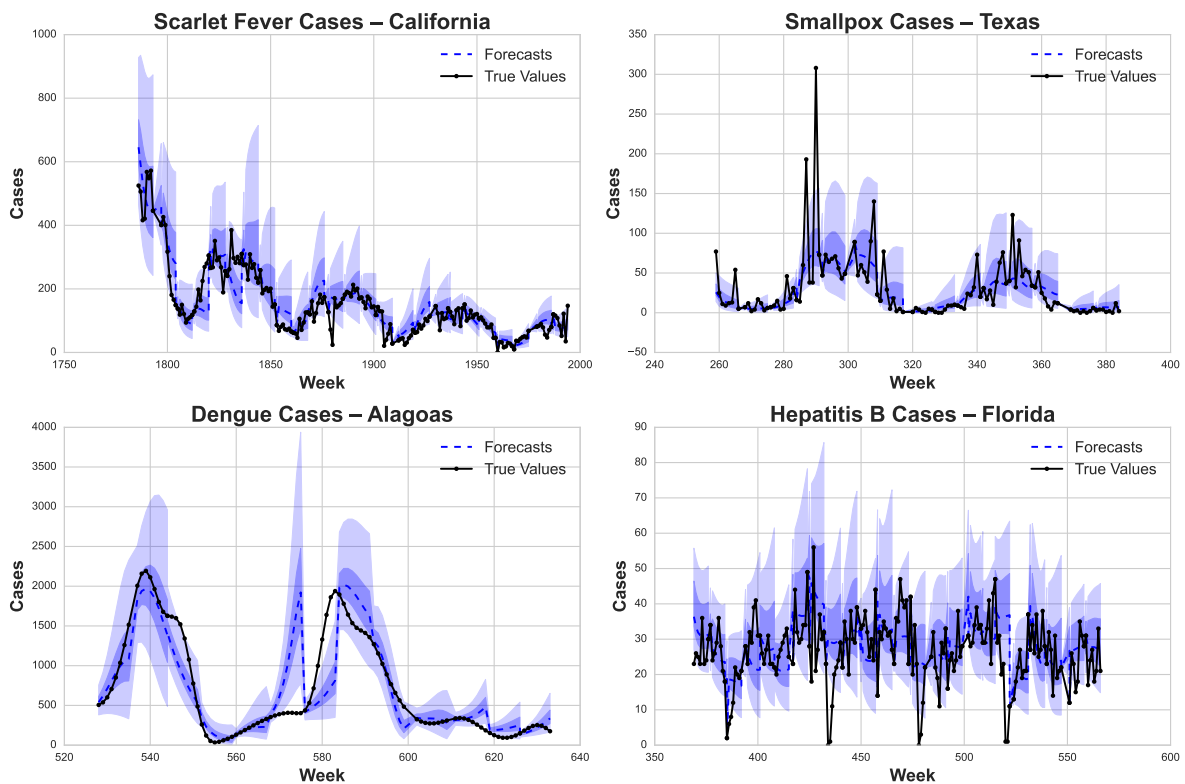


Figure 6: Forecasts with 50% CIs (dark blue shade) and 90% (light blue shade) demonstrate Mantis's calibration.

captures the true outcome roughly nine times out of ten. Such reliability enables evidence-based resource planning, from ventilator procurement to staffing decisions, with quantified confidence bounds that support both conservative and aggressive response strategies depending on acceptable risk levels.

The robustness of Mantis’s uncertainty estimates across diseases, time periods, and transmission modes underscores a key advantage of simulation-grounded training: by learning from diverse synthetic scenarios that span the full range of epidemiological uncertainty, the model internalizes realistic estimates of forecast confidence that transfer to real-world settings. This contrasts with models trained on limited historical data, which may exhibit over-confident predictions when encountering novel outbreak dynamics.

## D.2 Ablation Studies Confirm the Importance of Scale and Mechanistic Pre-training

To understand the key factors driving Mantis’s performance, we conducted two ablation studies examining the roles of architectural capacity and mechanistic pretraining in enabling accurate plug-and-play forecasting.

### D.2.1 Architectural Capacity Requirements

We first evaluated whether Mantis’s forecasting capabilities could be achieved with a simpler, more compact architecture. Using the same 400 million days of synthetic training data, we replaced Mantis’s hybrid CNN-transformer architecture with the dual-branch LSTM architecture from DEFSI [9]. This LSTM model contains approximately 200 times fewer parameters than Mantis, making it significantly more lightweight and computationally efficient.

Despite identical training data and procedures, the reduced architectural capacity led to substantially degraded performance. When evaluated on COVID-19 mortality forecasting across U.S. states, the LSTM architecture achieved mean absolute error (MAE) that was 89% higher than the full Mantis model. This demonstrates that while the synthetic training paradigm is powerful, it requires sufficient architectural capacity to effectively learn and generalize from the diverse mechanistic patterns encoded in the simulation data.

### D.2.2 Mechanistic Pretraining is Essential for Novel Outbreak Performance

To isolate the contribution of mechanistic pretraining, we trained the full Mantis architecture exclusively on real-world data, eliminating simulations from the training process. We evaluated on COVID-19 hospitalization forecasting. We implemented a rolling training strategy that provided the strongest possible baseline: the model was initially trained on the first few months of pandemic data, then progressively retrained with expanding datasets as more real-world observations became available. This approach mimics operational practice and ensures that the real-world-only model has access to all available historical information at each forecast point.

The results reveal the critical importance of mechanistic pretraining. When trained only on real-world COVID-19 data, forecast error increased by 262% compared to the simulation-pretrained Mantis model. This dramatic performance degradation reflects the fundamental challenge of learning outbreak dynamics from limited historical data during a novel pandemic. Real-world training data, even when accumulated over months, cannot capture the full spectrum of epidemic behaviors that might emerge. In contrast, the simulation-pretrained model draws from hundreds of millions of days of diverse outbreak scenarios, enabling it to recognize and extrapolate patterns even in unprecedented contexts.

These ablation results underscore the core insight behind Mantis: mechanistic pretraining enables models to internalize generalizable principles of epidemic dynamics that extend far beyond what can be learned from any single real-world outbreak. While architectural sophistication contributes to performance, the simulation-grounded training paradigm is the essential component that enables out-of-the-box generalization to novel diseases and outbreak contexts.